ABSTRACT

Simulation and Measurement of the Guided Microwave Spectrometry System

Joshua D. Daniliuc, M.S.E.C.E.

Mentors: B. Randall Jean, Ph.D., Yang Li, Ph.D.

Previously, a novel microwave measurement device known as the Guided Microwave Spectrometry (GMS) system was developed for retrieving properties of material under test (MUT) and non-destructively measuring the composition of various mixtures of known constituents. In this work, simulation and measurement studies on this GMS technology are presented to investigate how electromagnetic waves propagate in the structure. I will explain the wave propagation characteristics and how each individual component of the GMS contributes to the overall system response. The GMS system responses to both homogeneous and inhomogeneous materials inside the chamber are examined as well. Finally, I present ways to enhance GMS system performance by carrying out comprehensive parametric studies on both rectangular and circular GMS systems.

Simulation and Measurement of the Guided Microwave Spectrometry System

by

Joshua D. Daniliuc, B.S.E.C.E.

A Thesis

Approved by the Department of Electrical and Computer Engineering

_____

Kwang Y. Lee, Ph.D., Chairperson

Submitted to the Graduate Faculty of
Baylor University in Partial Fulfillment of the
Requirements for the Degree
of

Master of Science in Electrical and Computer Engineering

Approved by the Thesis Committee:

_____

B. Randall Jean, Ph.D., Chairperson

_____

Yang Li, Ph.D.

_____

Stephen McClain, Ph.D.

Accepted by the Graduate School

August 2013

_____

J. Larry Lyon, Ph.D., Dean

Page bearing signatures is kept on file in the Graduate School.

Copyright © 2013 by Joshua D. Daniliuc

All rights reserved

TABLE OF CONTENTS

List of Figures vi

List of Tables viii

Acknowledgments..... ix

CHAPTER ONE: Introduction..... 1

CHAPTER TWO: Background to GMS Technology and Spectral Response…..... 4

2.1 Measurement of Material Properties using DPK.....4
2.1.1 Measured Permittivity of Vegetable Oil.....7
2.1.2 Measured Permittivity of Water.....8
2.1.3 Measured Permittivity of Ultem.....8
2.2 Measurement of Spectral Response using GMS and VNA.....9
2.3 Interpretation of the Measured Spectral Response.....11

CHAPTER THREE: The Rectangular GMS..... 14

3.1 The Rectangular GMS Structure.....14
3.2 Simulation and Measurement of Pure Homogeneous Medium.....16
3.2.1 Simulation Setup of R-GMS with Air.....17
3.2.2 Simulation Results of R-GMS with Air.....20
3.2.3 Explanation of Theory for R-GMS with Air.....20
3.2.4 Simulation Setup of R-GMS with Vegetable Oil.....21
3.2.5 Simulation Results of R-GMS with Vegetable Oil.....22
3.2.6 Explanation of Theory for R-GMS with Vegetable Oil.....23
3.2.7 Simulation Setup of R-GMS with Water.....23
3.2.8 Simulation Results of R-GMS with Water.....24
3.2.9 Explanation of Theory for R-GMS with Water.....24
3.3 Simulation and Measurement of Binary Solutions.....25
3.3.1 R-GMS with 25% Water – 75% Oil.....25
3.3.2 R-GMS with 50% Water – 50% Oil.....26
3.3.3 R-GMS with 75% Water – 25% Oil.....27
3.4 R-GMS Parametric Studies.....28
3.4.1 Modifying the R-GMS Width and Length.....29
3.4.2 Modifying the Process Seal Width and Height.....30
3.4.3 Modifying the Process Seal Permittivity.....30
3.4.4 Modifying the Coupling Loop Structure.....33
3.5 Setting Benchmark for Ideal Energy Transfer.....34

CHAPTER FOUR: The Circular GMS..... 36

4.1 The Circular GMS Structure..... 36
4.2.1 Simulation Setup of C-GMS with Air.....39
4.2.2 Simulation Results of C-GMS with Air.....40
4.2.3 Explanation of Theory for C-GMS with Air.....40
4.2.4 Simulation Setup of C-GMS with Vegetable Oil.....42
4.2.5 Simulation Results of C-GMS with Vegetable Oil.....42
4.2.6 Explanation of Theory for C-GMS with Vegetable Oil.....43
4.2.7 Simulation Setup of C-GMS with Water.....43
4.2.8 Simulation Results of C-GMS with Water.....44
4.2.9 Explanation of Theory for C-GMS with Water.....45
4.3 C-GS with Oil and Water Binary Solutions..... 46
4.4 C-GS Parametric Studies……..... 48
4.4.1 Modifying the Distance Between the Process Seals.....49
4.4.2 Modifying the C-GMS Radius.....50
4.4.3 Modifying the C-GMS Length.....51
4.4.4 Modifying the Coupling Loop Structure.....51
4.5 Modifying the Port Position for the C-GMS…….....52

CHAPTER FIVE: Conclusion and Future Work.....56

BIBLIOGRAPHY…..... 59

LIST OF FIGURES

Fig. 1.1: Rectangular Waveguide…….....1
Fig. 2.1: Agilent Dielectric Probe Kit Setup with PNA.....5
Fig. 2.2: DPK Calibration Settings…….....6
Fig. 2.3: DPK High Temperature Probe……..…….....6
Fig. 2.4: Complex Permittivity of Vegetable Oil from 200 MHz to 10GHz.....7
Fig. 2.5: Complex Permittivity of Water from 200 MHz to 10GHz.....8
Fig. 2.6: Complex Permittivity of Ultem from 200 MHz to 10GHz.....9
Fig. 2.7: a) Rectangular GMS, b) Circular GMS 10
Fig. 2.8: a) Rectangular GMS Setup with VNA, b) Circular GMS Setup with VNA.....10
Fig. 2.9: Ideal GMS Spectral Response.....12
Fig. 2.10: R-GMS Filled with Water, Emphasis on Non-Ideal Characteristics.....13
Fig. 3.1: Modeled R-GMS.....14
Fig. 3.2: Dimensions of R-GMS Metal Body.....15
Fig. 3.3: Dimensions of R-GMS Process Seals, Backing Plate, and Coupling Loop.....16
Fig. 3.4: 50 Ohm Lumped Element and Waveguide Port.....17
Fig. 3.5: a) Original Global Mesh, b) Global Mesh with Subgridding.....18
Fig. 3.6: a) Time Domain Solver Parameters, b) S-Parameter Conditions.....19
Fig. 3.7: R-GMS Filled with Air.....20
Fig. 3.8: R-GMS with Oil, Non-Debye Results.....22
Fig. 3.9: CST Debye-Model Parameter Settings for Vegetable Oil.....23
Fig. 3.10: R-GMS Filled with Vegetable Oil.....23
Fig. 3.11: R-GMS Filled with Water.....25
Fig. 3.12: Water and Oil Solutions.....26
Fig. 3.13: R-GMS with 25% water, 75% oil.....27
Fig. 3.14: R-GMS with 50% water, 50% oil.....28
Fig. 3.15: R-GMS with 75% water, 25% oil.....29
Fig. 3.16: Modifying R-GMS Width.…….....30
Fig. 3.17: Modifying R-GMS Length…….....30
Fig. 3.18: Modifying R-GMS Process Seal Width.....31

Fig. 3.19: Modifying R-GMS Process Seal Height.....32
Fig. 3.20: Modifying Process Seal Permittivity.....33
Fig. 3.21: Modifying Coupling Loop Depth.....34
Fig. 3.22: Modifying Coupling Loop Height.....34
Fig. 3.23: Ideal Waveguide Ports.....…….....35
Fig. 4.1: Modeled C-GMS.....37
Fig. 4.2: Completed C-GMS system.....37
Fig. 4.3: Dimensions of C-GMS metal body.....38
Fig. 4.4: Dimensions of C-GMS process seals and coupling loop.....38
Fig. 4.5: Mesh setting for C-GMS filled with air.....39
Fig. 4.6: C-GMS filled with air.....40
Fig. 4.7: Mesh Setting for C-GMS Filled with Oil.....41
Fig. 4.8: C-GMS Filled with Vegetable Oil.....42
Fig. 4.9: Mesh Setting for C-GMS Filled with Water.....44
Fig. 4.10: C-GMS Filled with Water.....44
Fig. 4.11: Different Water and Oil Solutions.....46
Fig. 4.12: C-GMS with 25% water, 75% oil.....47
Fig. 4.13: C-GMS with 50% water, 50% oil.....48
Fig. 4.14: C-GMS with 75% water, 25% oil.....49
Fig. 4.15: Modifying C-GMS Process Seal Distance.....50
Fig. 4.16: Modifying C-GMS Radius.....51
Fig. 4.17: Modifying C-GMS Length.....52
Fig. 4.18: Modifying C-GMS Coupling Loop Depth.....52
Fig. 4.19: Modifying C-GMS Coupling Loop Height.....53
Fig. 4.20: a) Rotating port 180°, b) Spectra for rotating port 180°.....53
Fig. 4.21: C-GMS new port position, rotating port 90°.....54
Fig. 4.22: C-GMS new port position, rotating port 180°.....55

LIST OF TABLES

Table 1: Calculated Cutoff Frequency for Circular Waveguide Filled with Air.....44

Table 2: Calculated Cutoff Frequency for Circular Waveguide Filled with Oil….....46

Table 3: Calculated Cutoff Frequency for Circular Waveguide Filled with Water.....49

ACKNOWLEDGMENTS

I thank Dr. Jean for guiding, molding, and keeping me focused – all with a spirit of wisdom and grace. I also thank Dr. Li for his tremendous patience and generous advice throughout the whole research and revision process. Finally, I thank my family for their support, understanding, and encouragement throughout the entire course of my studies.

CHAPTER ONE

Introduction

A waveguide is a common structure in microwave engineering that is mainly used for the transmission of microwave energy. Waveguides are made in many variations in terms of designs such as rectangular, circular, and parallel plate waveguides [1]. The propagation characteristics of electromagnetic (EM) waves inside a waveguide are determined by the waveguide's physical dimensions as well as the materials filling the structure. For example, as shown in Fig. 1.1, dimension 'a' determines the cut-off frequency of a waveguide while dimension 'b' influences the waveguide power handling ability. The presence of higher permittivity materials also cause the cutoff frequency to shift lower in frequency, as will be shown in chapter three. Inversely, given the EM wave propagation characteristics in waveguide unit, it is possible to retrieve the material properties in specific frequency bands. This important observation leads to several microwave sensor designs including the Guided Microwave Spectrometer (GMS) system [2, 3].

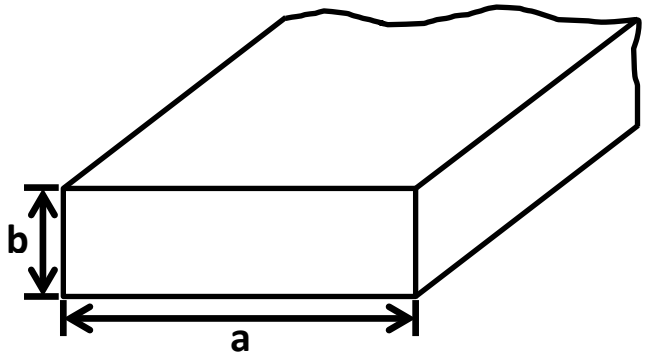

Fig. 1.1: Rectangular waveguide

A GMS system, which measures the spectral response of a waveguide structure to identify materials under test, has been successfully implemented in a variety of industrial applications: to measure materials such as oil or chemicals, to determine ratios of steam with water mixtures or ethanol with water mixtures, or to analyze the quality of food products such as pastes, dough, and ground meat. It is a non-destructive measurement tool that performs well with solids, liquids, and multi-phase materials in both online and offline processes. Furthermore, this system is an accurate and highly efficient measurement technique which can be implemented in real time.

Many applications for which the GMS technique has real value exist, but in spite of the demonstrated successes, developing this technology for all these applications is costly and time consuming. The current design method for this measurement system involves a cut and try procedure which often requires repeated laboratory measurements to observe how each modification alters the spectral response. This procedure not only becomes time intensive, but the costs can also increase as various system materials are sought out for compatibility with the material under test (MUT). For instance, the GMS process seal must be made from materials which meet health safety requirements in the food industry, high-pressure requirements in steam or oil plants, corrosion resistance requirements in a chemical facility, or which hold up to the highly abrasive nature of rocks within a batch of concrete as it flows by. To account for these limitations, the CST Microwave Studio simulation platform is used to develop these systems more easily [4].

The objective of this work is to develop a numerical simulation model using CST Microwave Studio for the rectangular and circular GMS systems available in our lab. Full wave simulation tools such as CST can provide several advantages over the traditional

design methods for the GMS: easier manipulation of the structure geometry, clearer identification of the contribution of each component, better understanding of propagation of waves inside the chamber, faster evaluation of performance, and lower cost of development. The performance of this tool will be tested against the performance of the rectangular GMS (R-GMS) and circular GMS (C-GMS), and once I demonstrate that the simulation results match measurement results for given experimental conditions, parametric studies will be performed to identify the contributions of each component within the GMS. I isolate each of the components to see what effect varying their dimensions, even in small increments, will have on the overall spectral response of the system for different types of MUT. This information should then be useful in knowing what features are important to the system design and which features are not as important.

This thesis is organized as follows: Chapter 2 provides a more in-depth background on the GMS and important related topics. It explains the measurement procedure, including a description of which equipment and experimental conditions are used. It will also describe how to interpret the graphical representation of the data obtained from the simulations and measurements for each GMS system; this will be essential for understanding the results from chapters 3 and 4. Chapter 3 presents the investigation that was done on the rectangular GMS, and Chapter 4 covers the circular GMS. Finally, Chapter 5 presents the conclusion and recommendations for future work.

CHAPTER TWO

Background to GMS Technology and Spectral Response

This chapter reviews the GMS measurement technique presented in three parts. The first section reviews studies done on the complex permittivity of the MUT - vegetable oil and Waco tap water - and also on the Ultem process seals [5] with an Agilent 85070E dielectric probe kit (DPK) [6]. The second section presents the instrumentation used to make each measurement, while illustrating how the measurement systems were arranged. The third section presents the spectral response obtained from the GMS measurements and identifies three main spectral parameters that will be observed throughout my studies.

2.1 Measurement of Material Properties using DPK

To facilitate understanding the properties of the GMS systems, the homogeneous materials of air, vegetable oil, and water were used for the MUT due to their well-documented properties. Vegetable oil has low molecular polarity and a low dielectric constant, while water is highly polar and has a high dielectric constant; the properties of every material combination that can exist in the measurement world fall within the range of the properties of oil and water, thus making these two materials ideal for the MUT.

The DPK system setup is shown in Figure 2.1, along with all the associated hardware and software. The DPK hardware was calibrated with the Agilent 85070E software that accompanied the instrument at its purchase [7], and an Agilent Performance Network Analyzer (PNA) [8] was used to obtain the permittivity measurements from 200 MHz to 13.5 GHz. Once the hardware was calibrated with the software settings in Figure

2.2, the high-temperature probe shown in Figure 2.3 obtained the real and imaginary part of the permittivity through a series of reflection measurements.

For the vegetable oil and water tests, the probe was partially submerged in the materials, and attention was given to ensure that pockets of air did not collect on the end of the probe since air pockets could alter the reflection characteristics. For the Ultem process seal tests, the probe was just placed as flat as possible against the flat surface of the seal. All the data was then plotted using MATLAB [9].

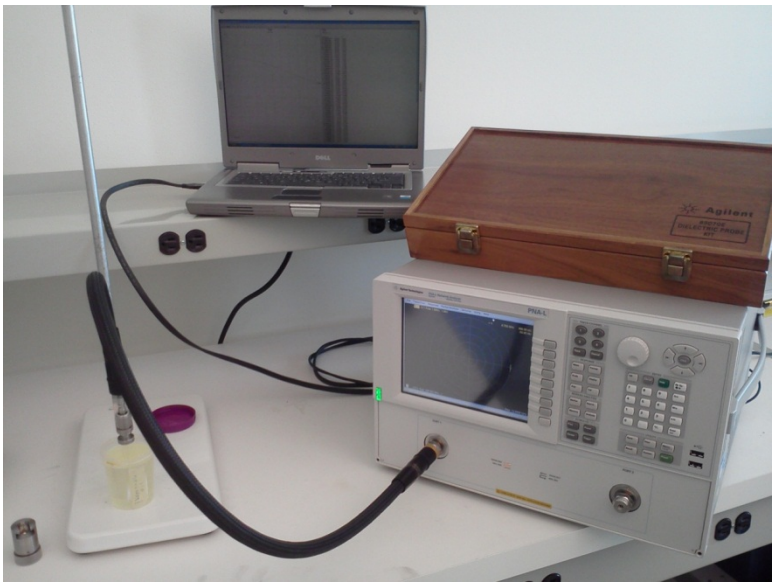

Fig. 2.1: Agilent Dielectric Probe Kit Setup with PNA

Most natural materials exhibit Debye behavior, where molecular materials attempt to orient themselves in the direction of an electric field (E-field) that is imposed upon the material [10]. This displacing force creates potential energy as molecules seek to return to their original position, and the fluctuating E-field causes the molecules to continuously rotate with the alternating field direction. Due to faster rotation at higher frequencies, the dipole may not have enough time to completely align itself with the rapidly fluctuating E-

field, which in turn decreases how efficiently a material can store energy at higher frequencies. As will be displayed in Figures 2.4 – 2.6, the real part of the complex permittivity indicates the stored energy within the medium and the imaginary part of the complex permittivity indicates the dissipation of energy within the medium.

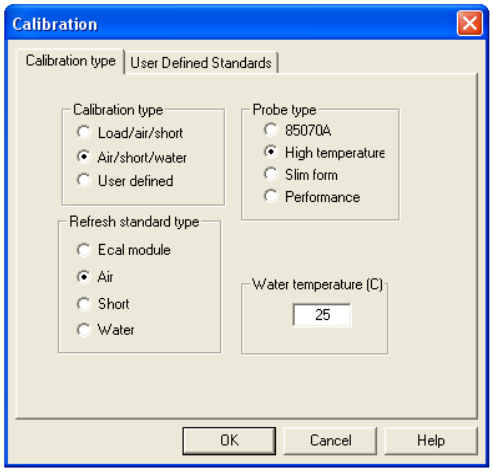

Fig. 2.2: DPK Calibration Settings

Fig. 2.3: DPK High Temperature Probe

2.1.1 Measured Permittivity of Vegetable Oil

The measurement data for the vegetable oil is shown in Figure 2.4. The real part of the permittivity of the oil was determined to be about 3.146 at 200 MHz and 2.504 at 10 GHz. The imaginary part of the permittivity remained relatively stable across the entire frequency range, starting at about 0.2178 at 200 MHz and raising slightly to 0.2575 at 10 GHz.

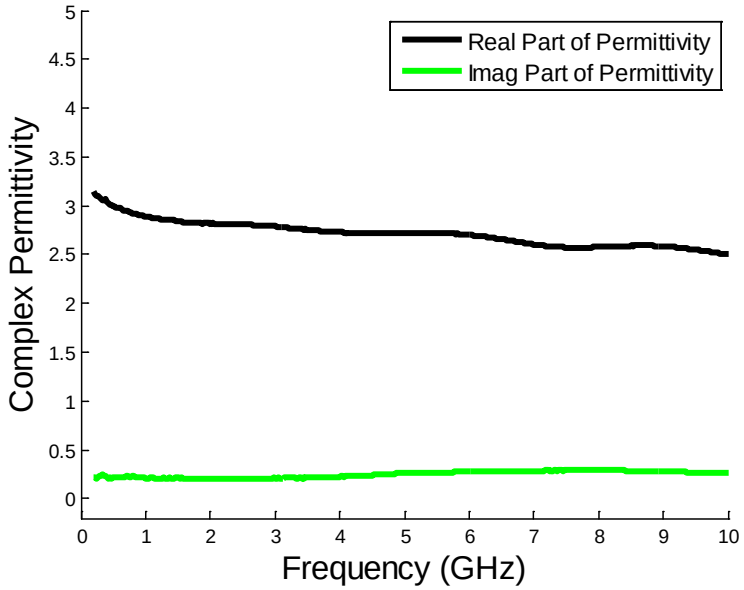

Fig. 2.4: Complex Permittivity of Vegetable Oil from 200 MHz to 10GHz

Also from Figure 2.4, the overall permittivity of the oil is not high on the dielectric constant scale, which means that its ability to store energy will be rather small as the molecular polarization occurs. It can be anticipated, however, that a benefit of oil will be to reduce any excess multipath phenomenon inside the closed waveguide cavity as signals become slightly attenuated when passing through this medium. This is opposed to an empty chamber where signals reflect off the metal walls continuously without any material in the way to attenuate them and decrease their strength.

2.1.2 Measured Permittivity of Water

The complex permittivity of water is shown in Figure 2.5, and the overall higher permittivity will produce a spectral response very different from that of oil. The real part of the permittivity starts at 81.03 at 200 MHz and gently slopes off to 59.02 at 10 GHz, and the imaginary part is 0.9169 at 200 MHz and 34.11 at 10 GHz. Water has a greater ability to store energy at lower frequencies, but Figure 2.5 shows how, as the imaginary part of the permittivity increases at higher frequencies, water dissipates more energy and is able to store less.

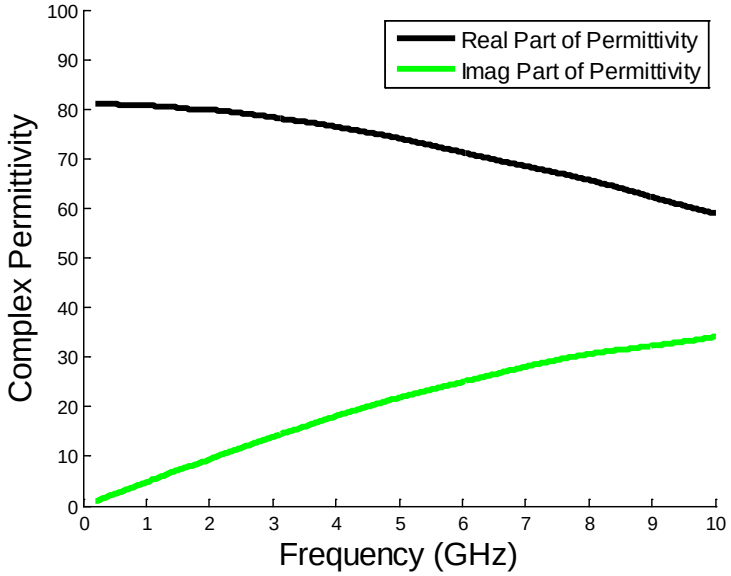

Fig. 2.5: Complex Permittivity of Water from 200 MHz to 10GHz

2.1.3 Measured Permittivity of Ultem

There exist many types of Ultem and the dielectric constant of each type ranges from as low as 3.05 to as high as 6 based upon how many additives are added to the material. The specific type of Ultem used for the study was initially unclear, but the DPK results in Figure 2.6 reveals that the real and imaginary part of the permittivity at 200 MHz is 3.283 and 0.0026, respectively, while the real and imaginary part of the

permittivity at 10 GHz is 3.049 and 0.247, respectively. This experimental permittivity result was then used in my software model.

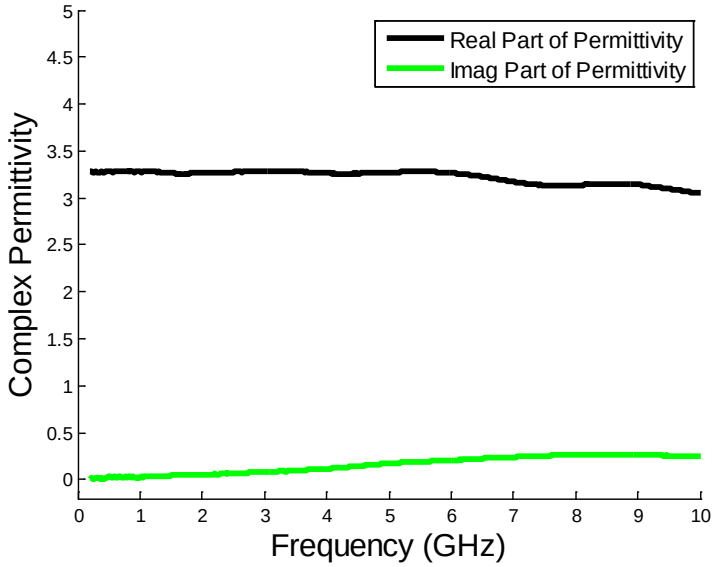

Fig. 2.6: Complex Permittivity of Ultem from 200 MHz to 10GHz

2.2 Measurement of Spectral Response using GMS and VNA

The rectangular GMS (R-GMS) and the circular GMS (C-GMS) are shown in Figure 2.7(a) and 2.7(b) and also together with the Agilent E5071B Vector Network Analyzer (VNA) [11] system set up in Figure 2.8(a) and 2.8(b). The VNA provides input signals over a frequency range of 300 kHz to 8.5 GHz and provides an output with 125db dynamic range. The data for each experiment is saved from the VNA through a Visual Basic for Applications (VBA) script which exports the complete S2P values from 300 kHz to 4 GHz. The S2P data contains the reflection and cross-transmission information between the two ports for each GMS, which means that four amplitude values in dB are obtained for each frequency point. Each S2P file was then opened on a desktop computer using MATLAB to externally post-process the information, and the final product was a plot of the data.

Fig. 2.7: a) Rectangular GMS, b) Circular GMS

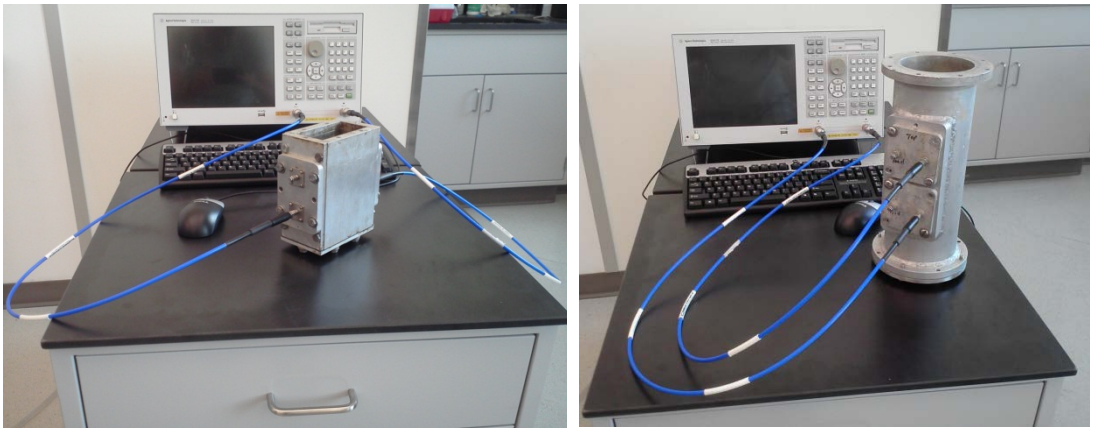

Fig. 2.8: a) Rectangular GMS Setup with VNA, b) Circular GMS Setup with VNA

The first measurement was with an empty GMS to account for the air case, and each chamber was also filled to the brim with either vegetable oil or water; these three sets of experiments will be referred to as the pure homogeneous medium measurements. An investigation was also made to observe how each GMS performs when the measurement chamber is filled with a non-homogeneous combination of oil and water in ratios of 25% water – 75% oil, 50% water – 50% oil, and 75% water – 25% oil; these

three sets of experiments will be referred to as the binary inhomogeneous measurements. For these binary inhomogeneous solutions, in order to make it easier to maintain uniformity between the laboratory measurements and the software simulations, the oil was allowed to rise to the top and thus there exists distinct boundary between the two materials. Future studies will look at oil and water mixed together with an emulsifier, and simulation studies can target the more complicated problem of working with solutions that have an equal distribution of permittivity throughout the chamber.

2.3 Interpretation of the Measured Spectral Response

The theoretical response for an arbitrary material with a Debye-type response inside an ideal GMS is shown in Figure 2.9 [3]. The horizontal axis displays the operating frequencies from near-DC to 4 GHz and the vertical axis displays the magnitude of the S_{21} in dB. In the ideal case, there is a degree of orthogonality between the three main material parameters – ε_s, σ , and τ.

The ε_s parameter is the static, low-frequency permittivity of any given material. Changes in ε_s cause the cutoff frequency to move left and right, as indicated by the dotted green line. Higher permittivity materials will have a lower cutoff frequency while lower permittivity materials will have a higher cutoff frequency. The region above the cutoff frequency is termed the passband region, while the region below the cutoff frequency is termed the cutoff region.

The σ parameter is the conductivity of the material, and changes in this variable cause the amplitude to shift up and down, as illustrated in the dashed red line. Higher conductivity materials will have higher amplitude, while lower conductivity materials will have lower amplitude.

The τ parameter is the molecular relaxation of the material, and an increase in this value will cause the slope to increase, as in the orange dash-dotted line. If no molecular relaxation is present in the material, the slope would remain flat in the higher frequency range.

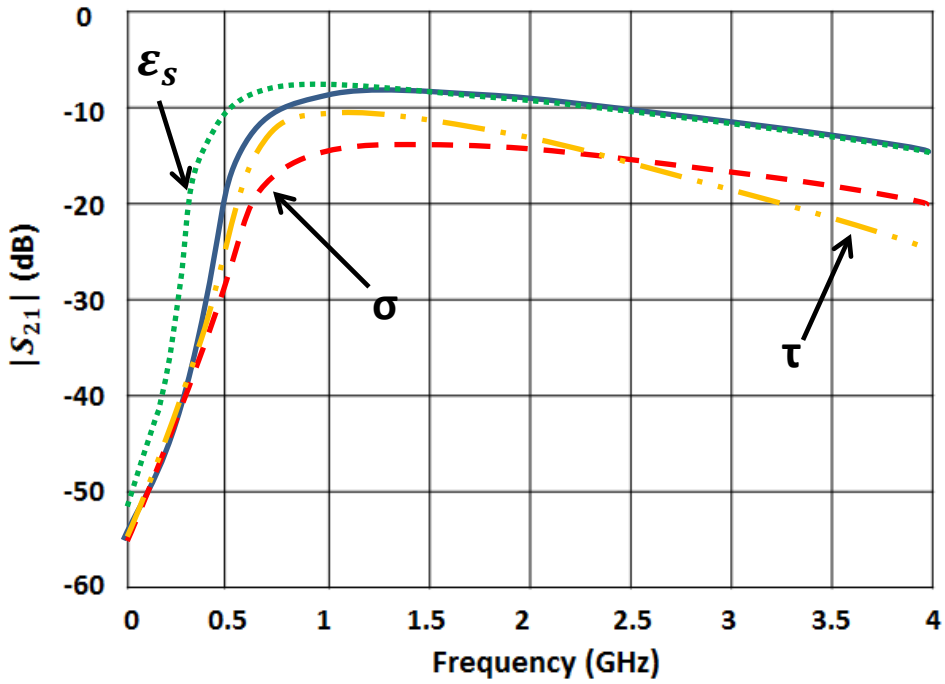

Fig. 2.9: Ideal GMS Spectral Response

The spectral response can take a variety of different shapes for different materials and real system response introduces many non-ideal features that must be accounted for in the design process. For instance, Figure 2.10 shows the output of a R-GMS filled with water, and there are a significant number of ripples in the 0.5 to 1.5 GHz region, as well as another perturbation at around 2.5 GHz. The CST tool would be used to identify which part of the GMS causes these ripples and to take appropriate measures to mitigate their effects conveniently. Ultimately, the design of a system that more easily extracts information about the material properties from the spectral response is desired.

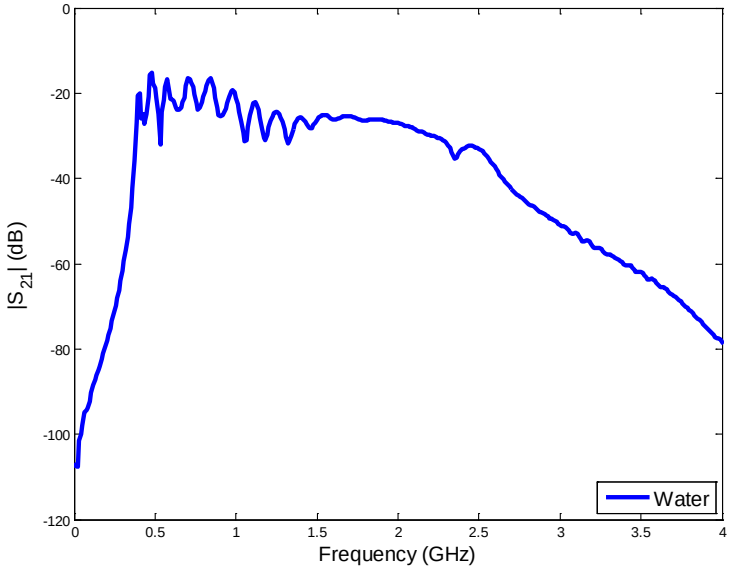

Fig. 2.10: R-GMS Filled with Water, Emphasis on Non-Ideal Characteristics

CHAPTER THREE

Simulation, Characterization, and Optimization of Rectangular GMS (R-GMS)

3.1 The Rectangular GMS Structure

The rectangular GMS (R-GMS) is made up of three main components: the waveguide body, the process seals, and the coupling loop. Each of the main components is emphasized in Figure 3.1 which illustrates how the components are arranged to function together; the corresponding dimensions are shown in Figures 3.2 and 3.3. First, start with a rectangular waveguide body that has port openings which are machined into

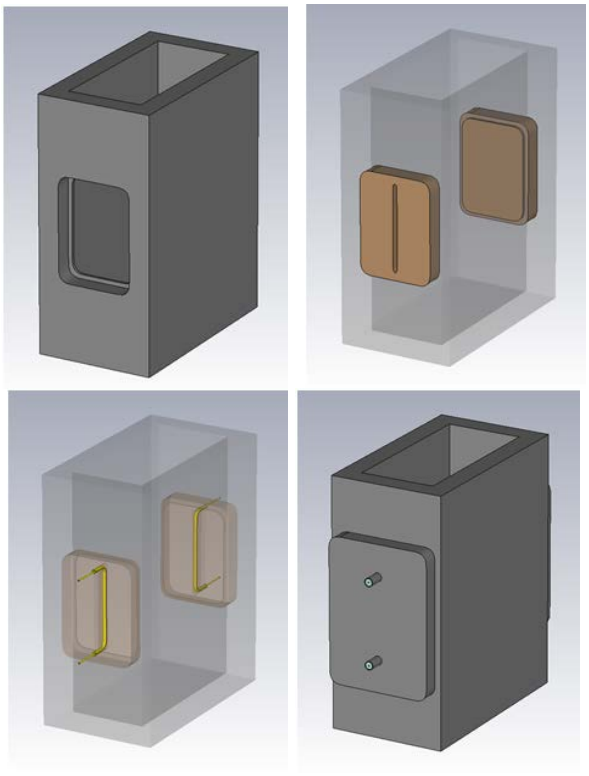

Fig. 3.1: Modeled R-GMS. From top left, clockwise: rectangular body, process seals, energy-coupling structure, GMS complete with backing plate

the narrow walls of the rectangular pipe section to accommodate the process seals. The ports are symmetrical about the vertical axis of the waveguide and will allow for the ability to transmit and receive microwave energy into and out of the measurement chamber. The energy travels across the pipe from one port to the other while passing through the material. The process seals have a rectangular cutout on the external facing side which will allow for insertion of the energy-coupling structure into it.

The energy-coupling structure, hereafter referred to as coupling loops, consists of a copper wire that has been shaped to fill the cutout on the process seal and has a transition to fit into standard SMA connectors, which will then be connected to the VNA. A backing plate is then mounted to each of the sides to isolate the system from any electrical or physical interference. These constitute the major details of the R-GMS and will be the focus for the parametric study.

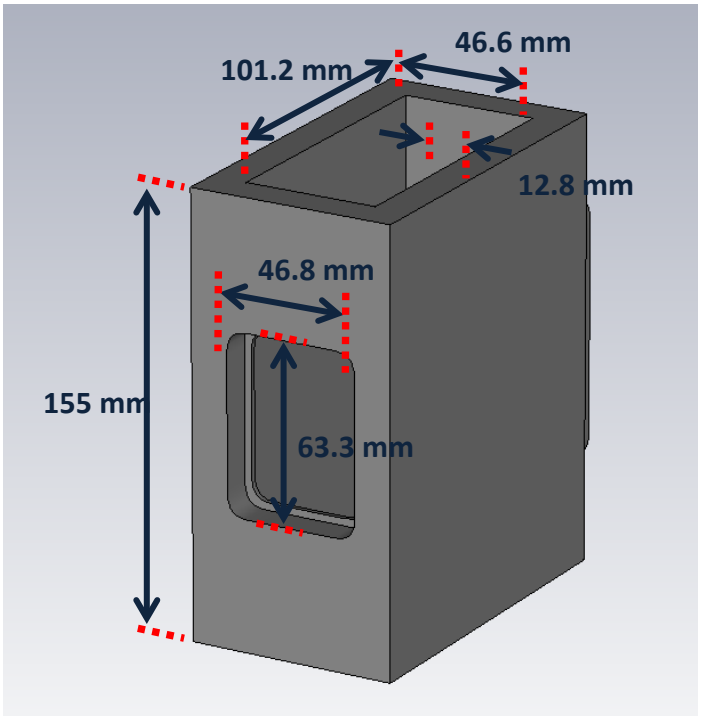

Fig. 3.2: Dimensions of R-GMS Metal Body

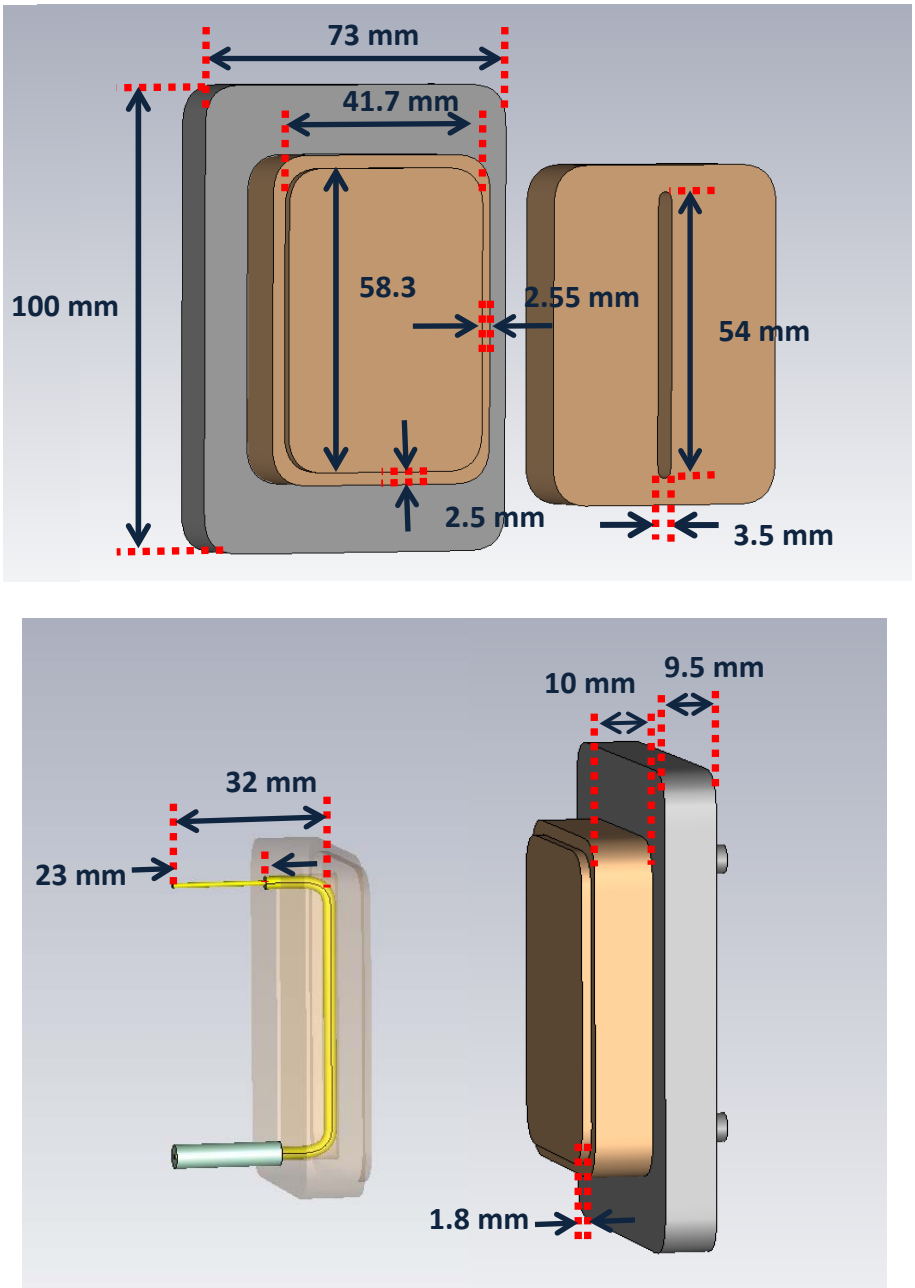

Fig. 3.3: Dimensions of R-GMS Process Seals, Backing Plate, and Coupling Loop

3.2 Simulation and Measurement of Pure Homogeneous Medium

The next step involved performing tests both in the laboratory and on the computer and comparing the results from the two to verify the accuracy of my software tool. In order to trust this model for parametric studies and for consideration of using the

GMS for new applications, it was necessary at this step to have the measurement results match the simulation results.

3.2.1 Simulation Setup of R-GMS with Air

The setup conditions for the R-GMS in CST involved setting the frequency range, the boundary conditions, the solver to be used, mesh setup and port conditions. The frequency range was set to sweep from 10 MHz to 4 GHz, while the boundary conditions were set to "open-(add space)" in the x, y, and z-directions. The GMS coupling loops were excited by waveguide ports over one of the coaxial ports, while the other end was terminated in a 50 ohm lumped element, as shown in Figure 3.4. For the waveguide port, the number of calculated modes was set to one. The R-GMS filled with air originally

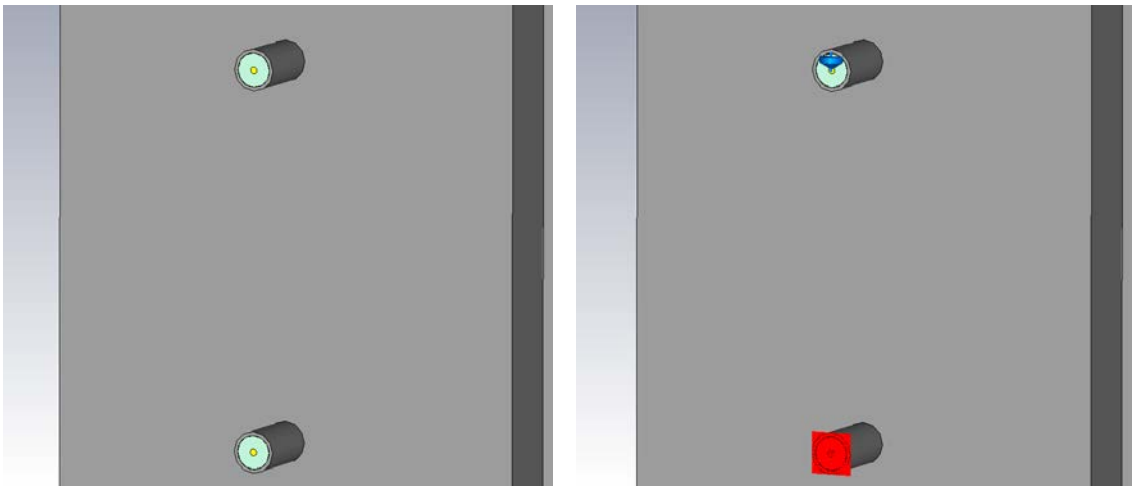

Fig. 3.4: 50 Ohm Lumped Element and Waveguide Port: a) Before, b) After

consisted of 4,625,280 mesh cells without any special mesh conditions, but since this project size became too large and took a long time to run, global subgridding was implemented which reduced the size down to 521,341 mesh cells. Figures 3.5(a) and

3.5(b) illustrate just how much more efficient CST's subgridding feature is, maintaining a finer mesh around critical areas with a lot of definition.

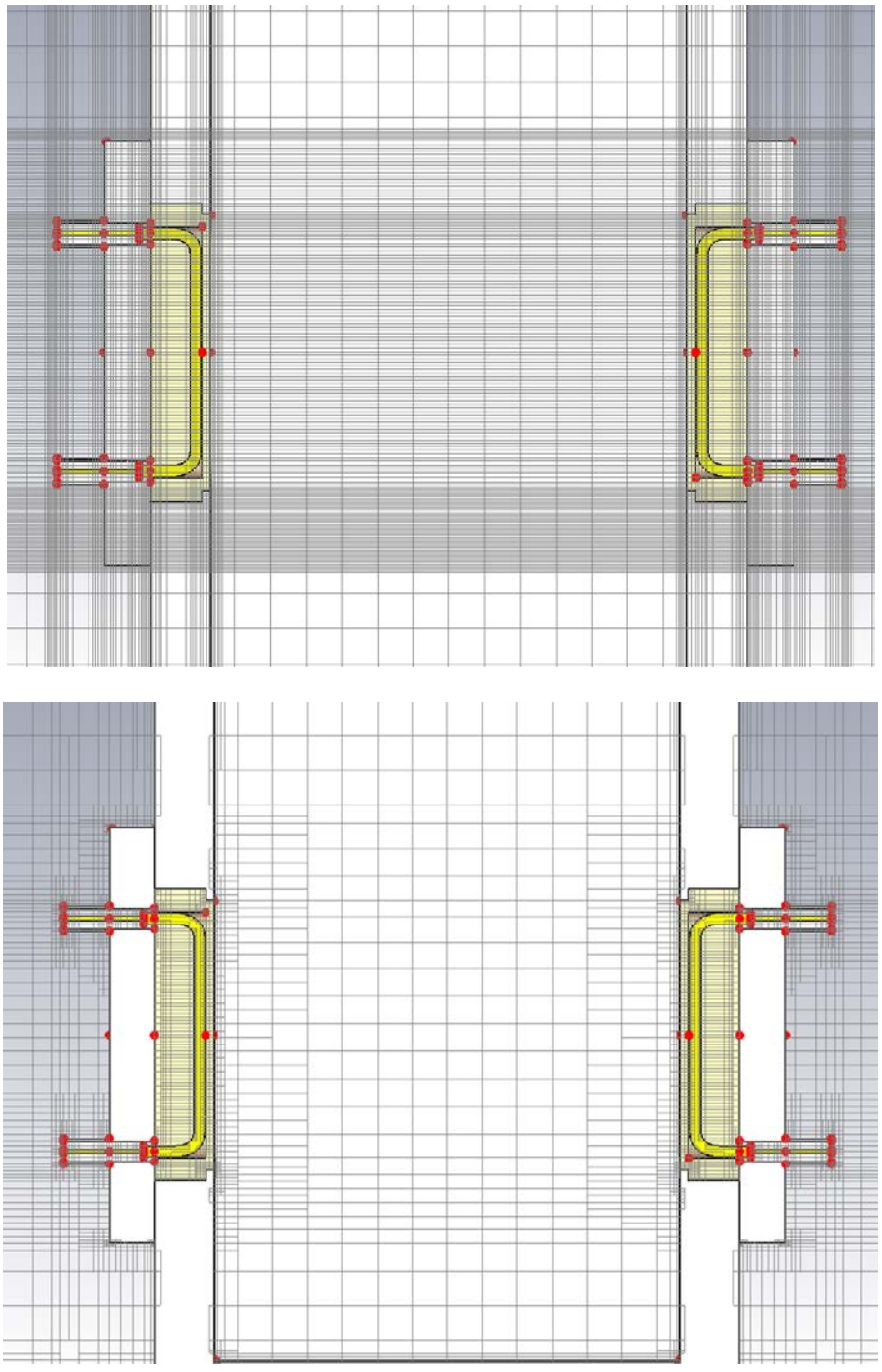

Fig. 3.5: a) Original Global Mesh (top), b) Global Mesh with Subgridding (bottom)

Additional techniques were applied in the time domain solver settings to speed up the processing time while still setting conditions for optimal performance. As summarized in Figure 3.6(a), the accuracy settings were set to -80 dB, which directs CST to continue to run the model until the energy level inside the measurement chamber falls 80 dB below the initial excitation levels. The inhomogeneous port accuracy option was checked to treat the coupling loop as a coaxial cable, and the results will be normalized to 50 ohms once finished. Figure 3.6(b) shows the S-Parameter symmetry feature was activated to speed up the processing time; here, symmetry condition was imposed on the S_{11} and S_{22} due to the symmetrical nature of the R-GMS, which halved the simulation time. Despite all these time saving strategies, the simulation took 53 hours and 35 minutes to meet the -80 dB energy dissipation requirements.

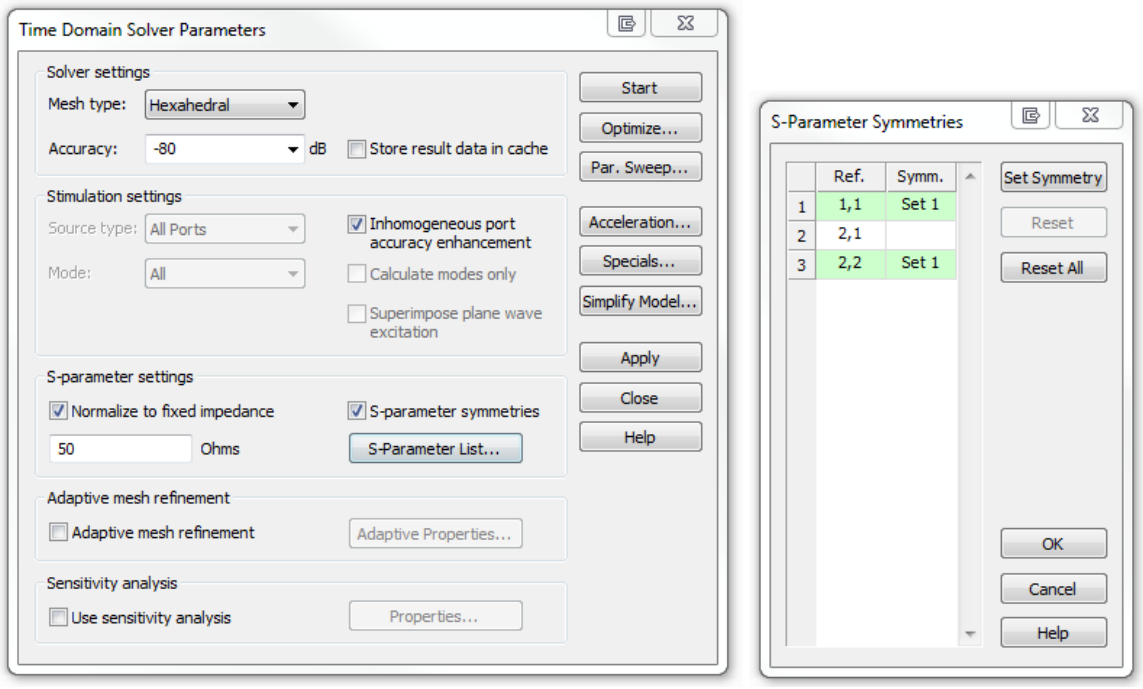

Fig. 3.6: a) Time Domain Solver Parameters, b) S-Parameter Conditions

3.2.2 Simulation Results of R-GMS with Air

The reflection results in Figure 3.7(a) indicate how efficiently energy is transferred into the measurement chamber through the coupling loop. The dotted line in the reflection waveform indicates the -10 dB line as a measure for how well energy is radiated from the coupling loop; from this, it is clear that the coupling loop does not propagate broadband energy well and has limited bandwidth. The cutoff frequencies occur closely in Figure 3.7(b) – 3.062 GHz in CST and 3.17 GHz in the measurement – but there is a discrepancy between the simulation and measurement in the cutoff region from 2.2 GHz to 3 GHz. This can be attributed to the inefficiencies in the coupling loop., compounded with the absorbing boundary conditions in CST which cannot fully simulate measurement conditions.

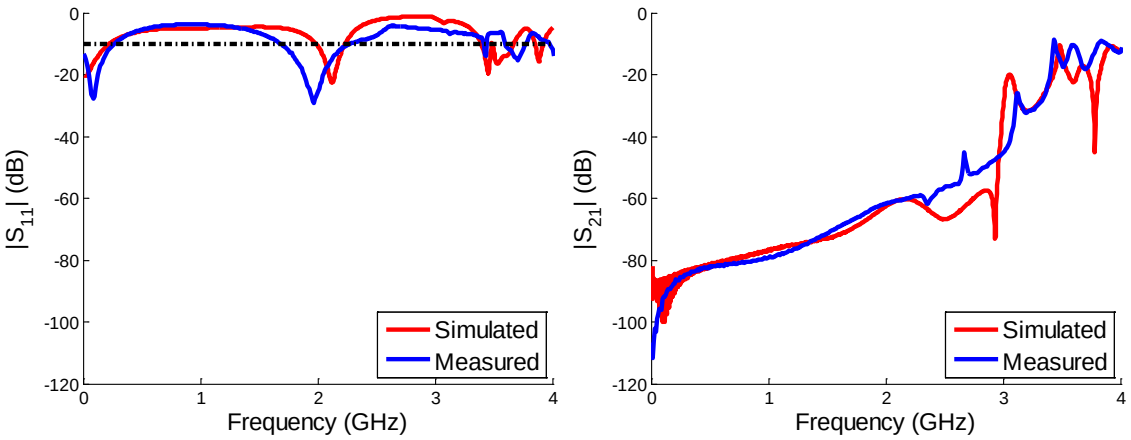

Fig. 3.7: R-GMS Filled with Air: a) S_{11} Response b) S_{21} Response

3.2.3 Explanation of Theory for C-GMS with Air

The theoretical calculation for the cutoff frequency for an empty R-GMS was derived to be 3.18GHz using Equation (3.1), where *a* (101.2 mm) and *b* (76.5 mm) are

the dimensions of the waveguide as shown in Figure 1.1 and ε and μ are the relative permittivity and permeability of the dielectric material, respectively, and *mn* is a given

$$(f_c)_{mn} = \frac{1}{2\pi\sqrt{\mu\varepsilon}}\sqrt{(\frac{m\pi}{a})^2 + (\frac{n\pi}{b})^2} \tag{3.1}$$

mode sought after [12]. The calculated cutoff frequency is 3.17 GHz based on the waveguide dimensions.

3.2.4 Simulation Setup of R-GMS with Vegetable Oil

In my initial approach to modeling the oil case, I did not account for the Debye properties of the permittivity and only used the real part of the complex permittivity; real part was maintained at a constant value of 2.8 across the frequency range from 10 MHz to 4 GHz. From Figure 3.8 it can be seen that the results were unsatisfactory, and after much investigation I realized that this was because there was no imaginary part of the permittivity, which is important to proper modeling of our system. I then incorporated the DPK oil permittivity data into my CST model using the CST Debye-modeling feature in the material settings for oil, which uses Equation (3.2) to plot Debye properties as a

$$\varepsilon_r(\omega) = \varepsilon_\infty + \frac{\varepsilon_{static} - \varepsilon_\infty}{1 + j\omega t_0} \tag{3.2}$$

function of frequency. Figure 3.9 summarizes the values for the infinite permittivity (ε_∞), the static permittivity (ε_{static}), and the relaxation time (t_o), which were chosen by trial and error until the simulated Debye plot matched the measured Debye plot.

The CST R-GMS model filled with oil consists of 4,398,240 mesh cells without special mesh conditions, but with subgridding it was reduced to 544,075 mesh cells. As in the air case, accuracy settings were set to -80 dB, the results were normalized to 50

ohms, and the S-Parameter symmetry feature was activated. The simulation took 3 hours and 19 minutes to meet the -80 dB energy dissipation requirements, which is a dramatic time reduction compared to the air case. This is likely due to oil's partially lossy characteristics, combined with lower energy storage capabilities, which allows the overall energy inside the chamber to fall below the -80 dB levels much more quickly.

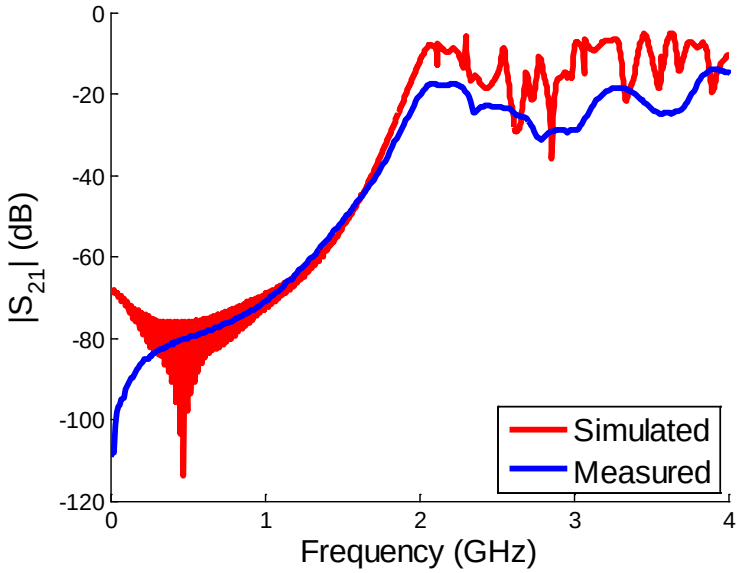

Fig. 3.8: R-GMS with Oil, Non-Debye Results

3.2.5 Simulation Results of R-GMS with Vegetable Oil

The transmission information from Figure 3.10(b) shows a dramatic improvement in the simulation results with the implementation of the Debye model for the oil. The remarkable comparison between the measurement and simulation indicates that our system is sensitive to minor changes in dielectric properties, even with low loss materials like oil. The cutoff frequency has shifted lower to around 2.085 GHz

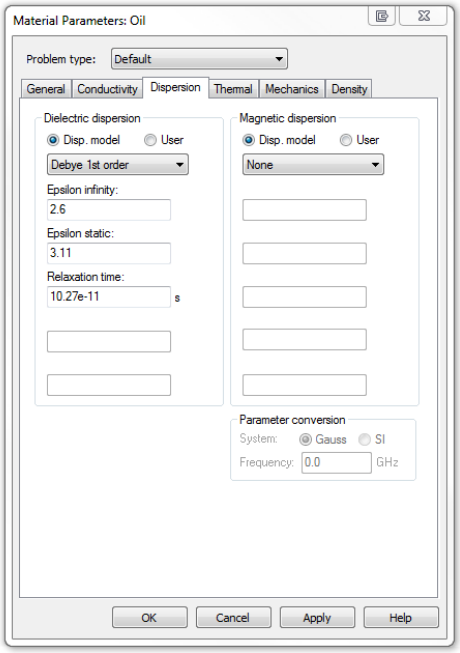

Fig. 3.9: CST Debye-Model Parameter Settings for Vegetable Oil

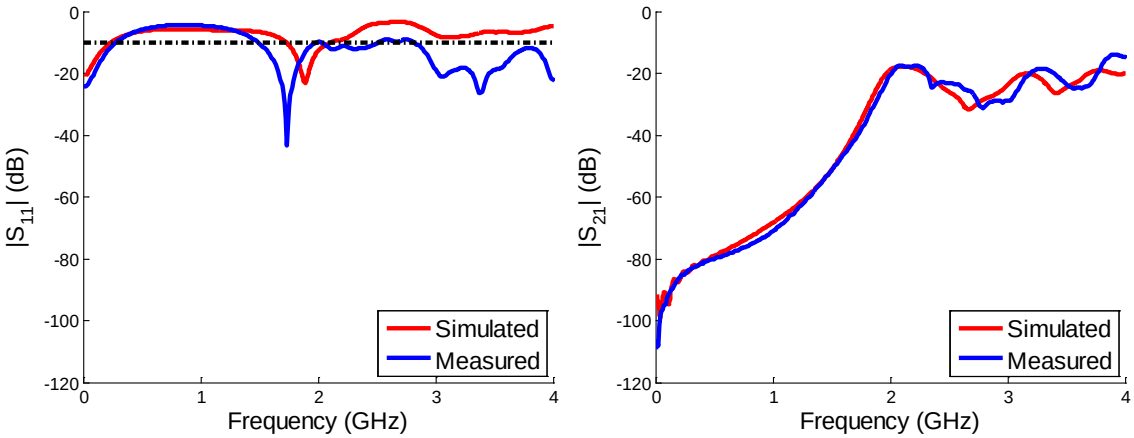

Fig. 3.10: R-GMS Filled with Vegetable Oil: a) S_{11} response b) S_{21} response

3.2.6 Explanation of Theory for C-GMS with Vegetable Oil

As mentioned in chapter two, the GMS cutoff characteristic depends on waveguide dimension and on the complex permittivity of the MUT inside the waveguide chamber. From Equation (3.1) the cutoff frequency would be dictated by the inverse of

the square root of the relative permittivity of a given material filling the waveguide. In this instance with oil, the real part of the permittivity is set to 2.75, which drives the cutoff frequency down to 1.912 GHz. Therefore the entire spectrum can be expected to shift lower in frequency when higher permittivity materials are placed in the GMS.

3.2.7 Simulation Setup of R-GMS with Water

CST already had a water Debye model in its material library, so their water was used. The CST R-GMS model filled with water consists of 10,000,485 mesh cells without any special mesh conditions, and with subgridding it was reduced to 2,253,800 mesh cells. The other settings were the same as with the air and oil cases and the simulation took 55 hours and 7 minutes to run to completion.

3.2.8 Simulation Results of R-GMS with Water

The reflection characteristics from Figure 3.11(a) show that the coupling loops are radiating rather well up until about 2.6 GHz. In Figure 3.11(b) the cutoff frequency has shifted lower in frequency to 0.394 GHz, and there are ripples up to 1.4 GHz in the passband region. Also, above around 2 GHz the passband signature begins to attenuate rather quickly, an attribute of the high relaxation time that water has.

3.2.9 Explanation of Theory for R-GMS with Water

For the water case the theoretical cutoff frequency is about 0.353 GHz according to (3.1) due to the very high dielectric constant of water which is around 78.2 at room temperature. The model looks to be very reliable in the lower frequencies where the modes line up very well, but it does not perform quite as well at higher frequencies where the coupling loop fails to radiate. At the lower frequencies CST does not have quite the

dynamic range of the VNA, but this is not a problem since the noise floor appears at around -80 dB in typical situations.

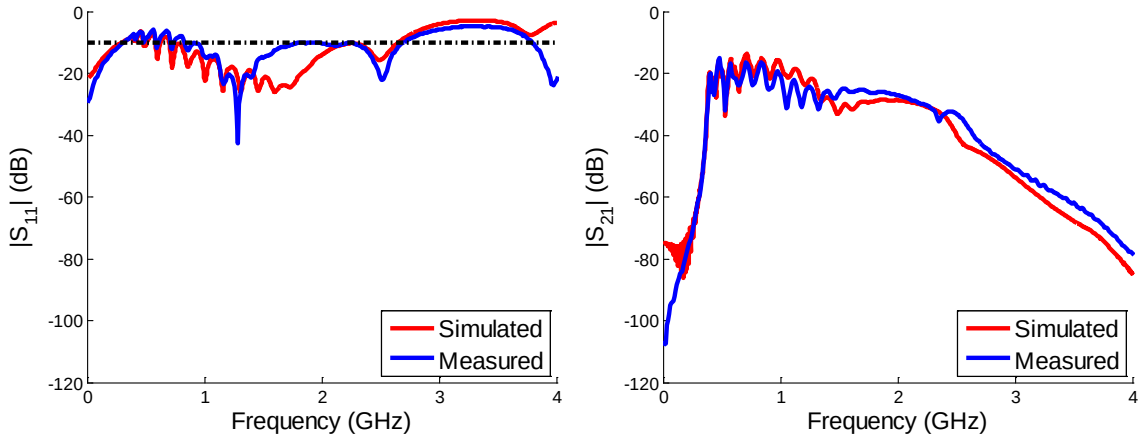

Fig. 3.11: R-GMS Filled with Water: a) S_{11} response b) S_{21} response

3.3 Simulation and Measurement of Binary Inhomogeneous Solutions

The results from Section 3.3 for the air, oil, and water cases are satisfactory, but before moving on to parametric studies the GMS tool must demonstrate that it detects different combinations of oil and water. As mentioned previously, these are the binary solutions shown in Figure 3.12 which consist of the 25% water – 75% oil, 50% water – 50% oil, and 75% water – 25% oil experiments. One point to make is that the full two-port S-Parameter data is presented in this section whereas in the previous sections only the S_{11} and S_{21} was given due to the imposed symmetry conditions. The oil and water were allowed to maintain a distinct separation to simplify the modeling, but future studies would simulate the more practical scenario of oil and water mixed together with an emulsifying agent.

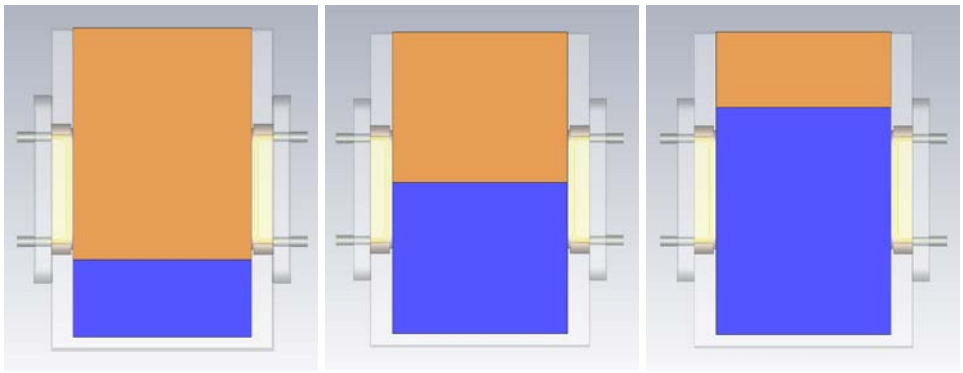

Fig. 3.12: Water and Oil Solutions: a) 25% water, 75% oil, b) 50% water, 50% oil, c) 75% water, 25% oil

3.3.1 R-GMS with 25% Water – 75% Oil

The 25% water and 75% oil case took 13 hours and 57 minutes to run to completion, with the same project setup as done in Section 3.2. Figure 3.13 summarizes the results showing a good match between the simulation and the measurement. The transmission response reveals that there are two cutoff frequencies, that of water and that of oil, at their respective frequencies. This indicates that the energy in the waveguide takes different paths through the materials in the waveguide, and travels at a different speed through the water than through the oil.

3.3.2 R-GMS with 50% Water – 50% Oil

Using the same setup settings as in Section 3.2, the 50% water and 50% oil case took 13 hours and 5 minutes to run to completion. Figure 3.14 shows a good match between the simulation and the measurement, with some deviation at frequencies higher than 2.6 GHz. The lower frequencies demonstrate that the modes are accounted for in the model, so I have confidence in this model at lower frequencies. It is evident that water and oil are both represented from the fact that the cutoff frequency is that of water, but the higher frequencies have the molecular relaxation of the oil.

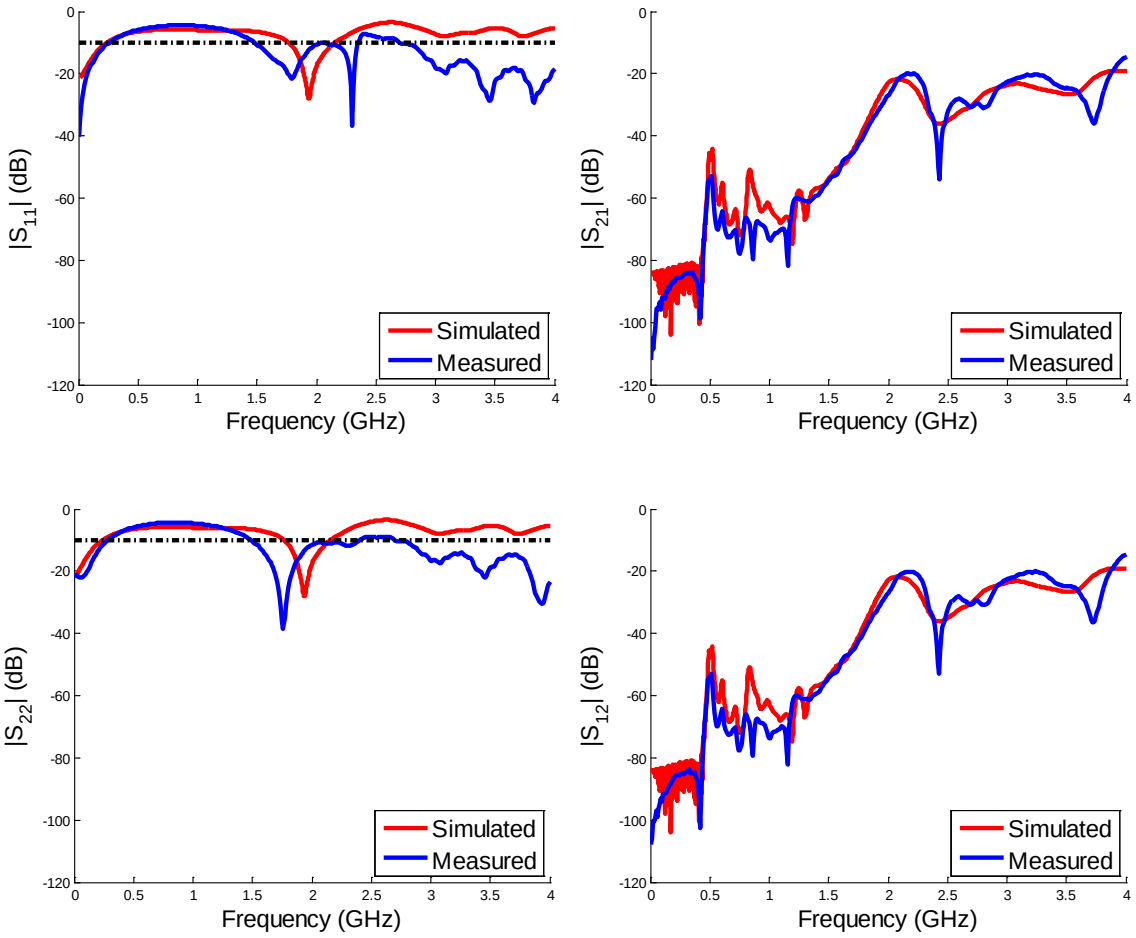

Fig. 3.13: R-GMS with 25% water, 75% oil. From top left: a) S_{11} , b) S_{21} , c) S_{22} , d) S_{12}

3.3.3 R-GMS with 75% Water – 25% Oil

The 75% water and 25% oil case took 23 hours and 14 minutes to run to completion. There is a good alignment of the modes in the transmission cases, with slight differences in the attenuation. The presence of oil is virtually unnoticeable in this solution; in a practical situation where water is flowing through a pipe, if an occasional slug of oil passes through the pipe it will not be easily noticed. Contrast this with the 25% water and 75% oil case in Section 3.3.1, where a slug of water in an oil filled pipe will certainly be noticeable from the spectral response.

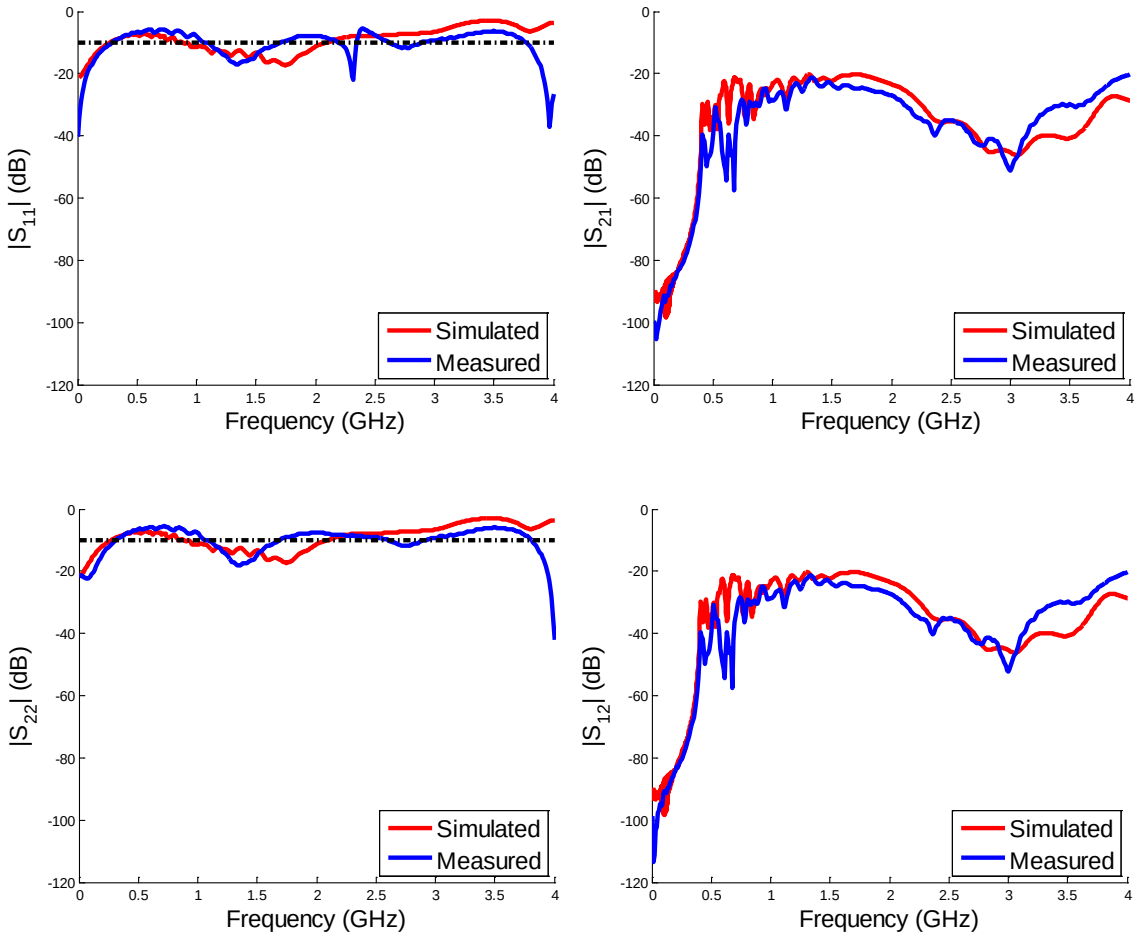

Fig. 3.14: R-GMS with 50% water, 50% oil. From top left: a) S_{11} , b) S_{21} , c) S_{22} , d) S_{12}

3.4 R-GMS Parametric Studies

I showed in the previous sections how the R-GMS model performs well from the simulation and measurement studies, so next I moved to performing parametric studies on the individual GMS components. The study was performed on the waveguide dimensions, the process seal dimensions, the process seal permittivity, and the coupling loop dimensions – all with the goal of seeing how variations in these qualities altered the spectral response.

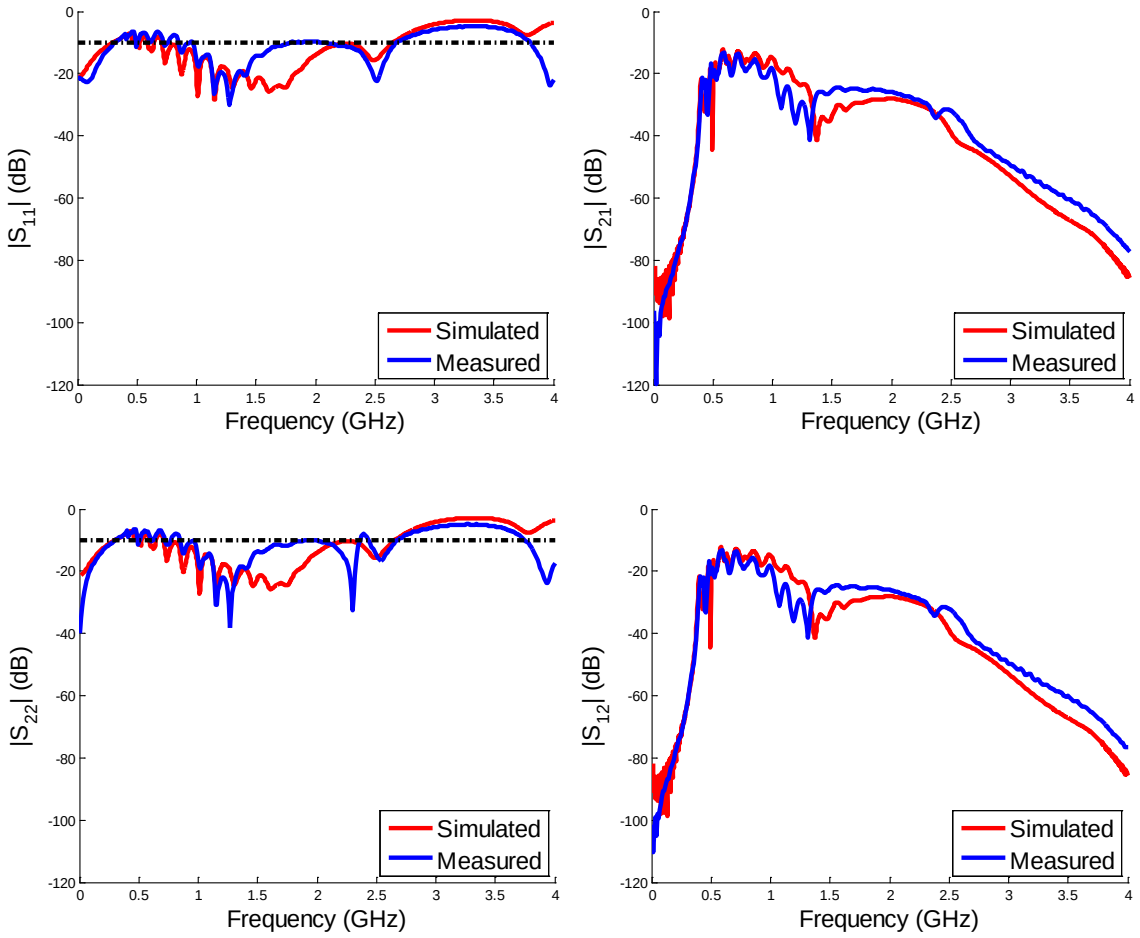

Fig. 3.15: R-GMS with 75% water, 25% oil. From top left: a) S_{11} , b) S_{21} , c) S_{22} , d) S_{12}

3.4.1 Modifying the R-GMS Width and Length

Figures 3.16 and 3.17 show the effects of modifying the width and length of the R-GMS. The results for changing the width meets the expectation for influencing the cutoff frequency, where increasing the width decreases the cutoff frequency while decreasing the width increases the cutoff frequency. Changing the length only affects the signal strength in the cutoff region, where greater lengths causes a sharper cutoff condition. This information could be useful when considering that calibration for each GMS sensor depends on the conditions particular to each sensor. This tool can be used to

transfer the calibration from one system to another for the same material type; quicker adjustments for the calibration between different pipe sizes can also be made.

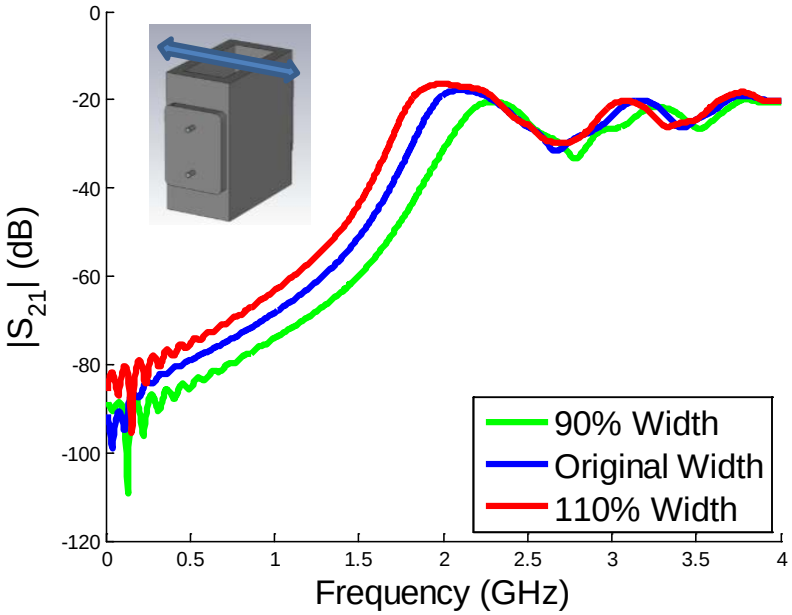

Fig. 3.16: Modifying R-GMS Width

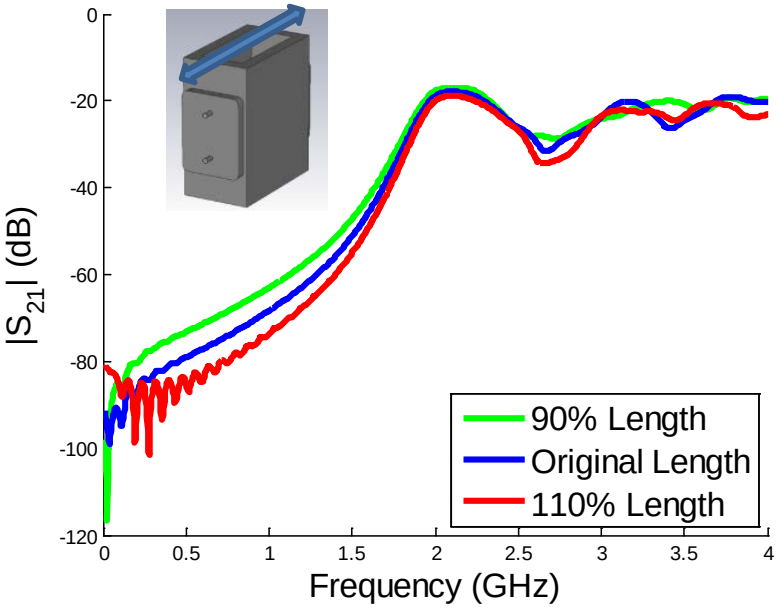

Fig. 3.17: Modifying R-GMS Length

3.4.2 Modifying the Process Seal Width and Height

Modifying the width of the process seal 10% from the original width has virtually no effect on the overall system response, as shown in Fig. 3.18. This indicates that the width of the process seal has no significant impact on the signal quality, which is particularly advantageous for situations where a smaller process seal area is desired, as in high-pressure applications. Figure 3.19 shows that changes in the height cause a lot of changes above 2.5 GHz, which indicates that energy coupling is greatly affected by this change.

3.4.3 Modifying the Process Seal Permittivity

Changing the process seal material will be necessary for different applications. For instance, corrosive chemical applications require the process seal to be made from material that does not get dissolved by the chemical, and applications which measure abrasive materials should have process seals that can withstand the rigors of that harsh environment.

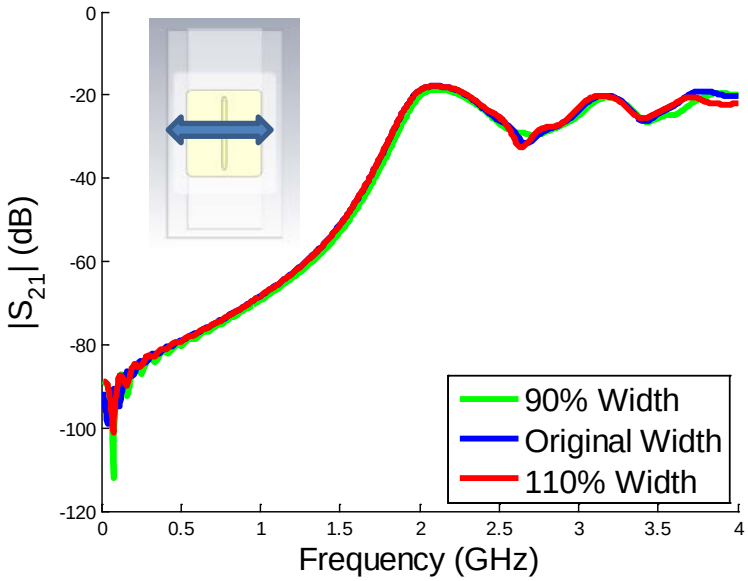

Fig. 3.18: Modifying R-GMS Process Seal Width

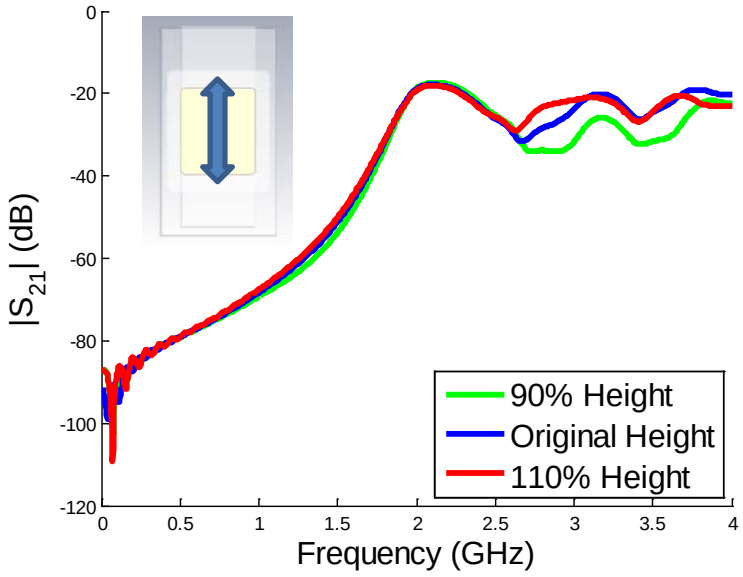

Fig. 3.19: Modifying R-GMS Process Seal Height

Figure 3.20 shows the effects of varying the permittivity of the process seal. As the permittivity increases, the intrinsic impedance of the process seal decreases according to Equation (3.3). This means that the coupling loop now will have a lower impedance match with higher permittivity process seal material. Also, a higher dielectric constant slows

$$\eta = \sqrt{\frac{\mu}{\varepsilon}} \tag{3.3}$$

down the phase velocity of the energy according to Equation (3.4), which results in the electrical length of the coupling loop becoming longer. With a longer effective probe length, the frequency at which problems begin to start goes down, and this is evident in the

$$v_p = \frac{1}{\sqrt{\mu\varepsilon}} \tag{3.4}$$

spectra results. I have demonstrated that the coupling loops are the source of error by changing their effective length by changing the permittivity of the process seal.

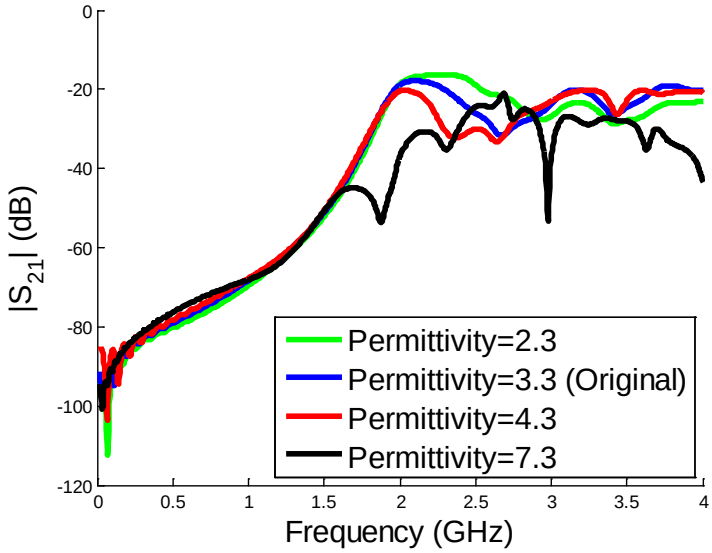

Fig. 3.20: Modifying Process Seal Permittivity

3.4.4 Modifying the Coupling Loop Structure

As concluded in the previous section, the coupling loop is a primary source of error, and the studies in this section will seek to gather more information. This parametric study involves adjusting the distance of the coupling loop from its default position and moving it closer to the backing plate, as summarized in Figure 3.21. It also involves decreasing the height of the two stubs of the coupling loop, as in Figure 3.22.

When decreasing the distance between the backing plate and the coupling loop, the capacitance between the two increases which causes the impedance of the coupling loop to decrease. As the coupling loop gets closer to the backing plate, more of the power is contained in that decreasing space so that less energy fringes out into the material. Ultimately, the signal strength becomes weaker as the coupling loop approaches closer.

Decreasing the height of the two legs of the coupling loop, as in Figure 3.22, performs similarly as decreasing the depth. There is still no change in the cutoff

frequency, which proves the robust ability of the GMS to not be affected by energy coupling methods.

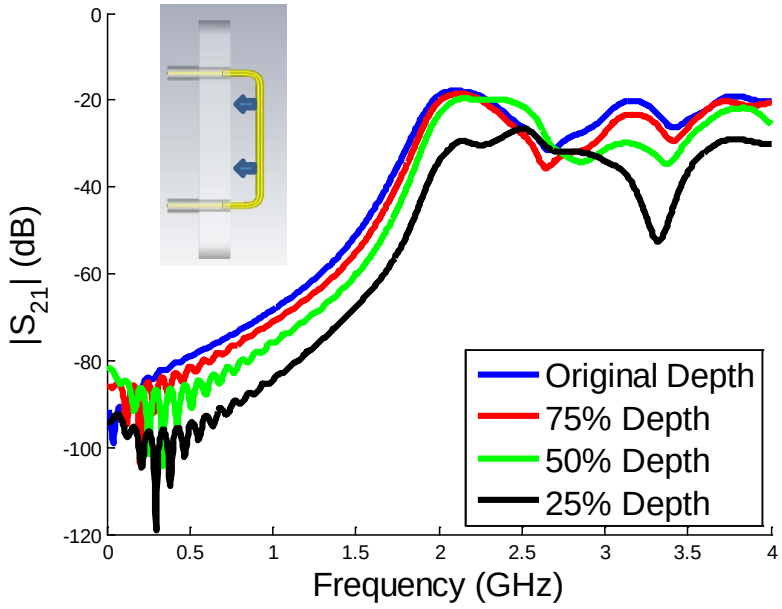

Fig. 3.21: Modifying Coupling Loop Depth

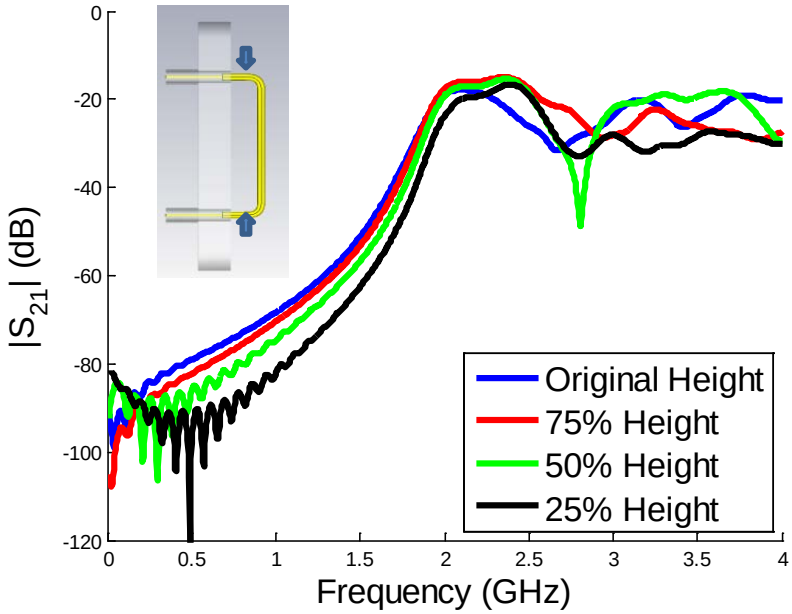

Fig. 3.22: Modifying Coupling Loop Height

3.5 Setting Benchmark for Ideal Energy Transfer

The main takeaway from the parametric study is that the coupling loop has some limitations on radiating broadband energy. This section looks to see how to improve system performance by finding better was to transfer energy into and out of the system. I do not present alternative energy coupling structures, but I do create a benchmark to show how the current coupling loop design compares with an ideal energy transfer design. Here, I replaced the existing excitation structure and replace it with ideal waveguide ports. These ports fit the dimension of the process seal window and do not have any limitations, and Figure 3.23 shows the modification as well as the results. Clearly, the ideal signal presents maximum information about the water filling the measurement chamber, and future coupling loops should seek to get as closet to this as possible.

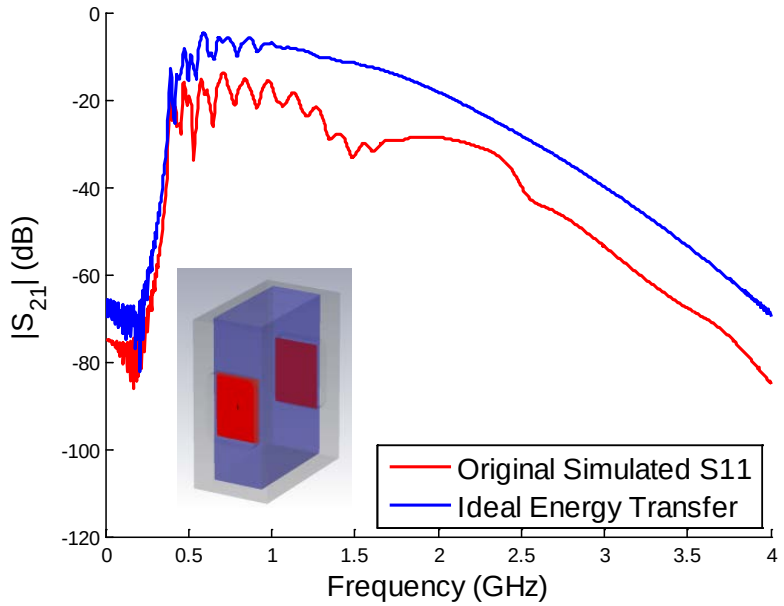

Fig. 3.23: Ideal Waveguide Ports

CHAPTER FOUR

Simulation, Characterization, and Optimization of Circular GMS (C-GMS)

4.1 The Circular GMS Structure

Unlike the R-GMS, the circular GMS (C-GMS) measurement chamber is round and the design and orientation of the process seals is different. The circular design allows the C-GMS to readily attach to pipes of the same radius, whereas a R-GMS would require a pipe transition to connect the rectangular body to a round pipe. Recall from Figure 3.1 that the R-GMS has ports on opposite ends of the waveguide; conversely, the C-GMS has both ports on the same side of the waveguide, as shown in Figure 4.1. This design is intentional and takes into account the properties of the circular waveguide, where propagation is down the axis of the pipe rather than across the axis of the pipe as in a rectangular waveguide. For a rectangular waveguide, the parallel plate walls reflect energy from one side to the other while the top and bottom plates determine the cutoff frequency. However, in the circular waveguide, cutoff frequency is not determined by such plates but rather by the diameter of the pipe.

Figure 4.1 breaks down the steps to how this system was created, Figure 4.2 shows the entire system as a completed unit, and Figures 4.3 and 4.4 show the components with their corresponding dimensions. In creating the C-GMS, first a pipe is extruded (Fig 4.1a) and a panel mount is then attached along the outside of the pipe. This panel mount provides a flat surface for the process seals to be inserted into (Fig 4.1b). Once the process seal holes are created (Fig 4.1c), Ultem process seals are put into place and end caps are inserted (Fig 4.1d). The end caps serve to create a closed system as

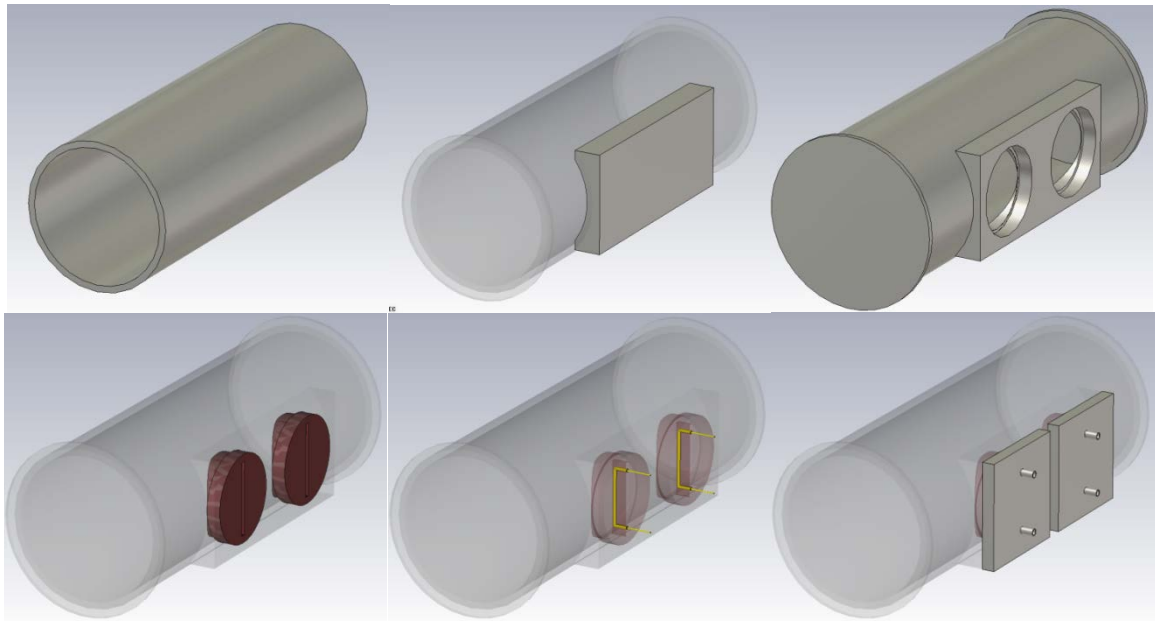

Fig. 4.1: Modeled C-GMS: a) Extruded pipe, b) Mounted panel, c) Process seal holes in panel, d) Ultem process seals, e) coupling loops, f) backing plate

opposed to an online process flow system. The excitation structure is similar to that used in the R-GMS, and these coupling loops are inserted into the process seal (Fig 4.1d). Finally the backing plates were inserted to close off the system, as shown in Fig 4.1f.

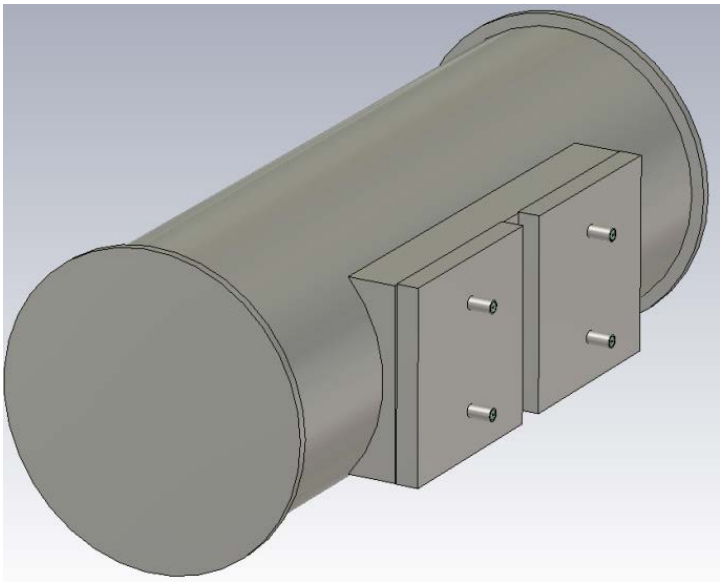

Fig. 4.2: Completed C-GMS system

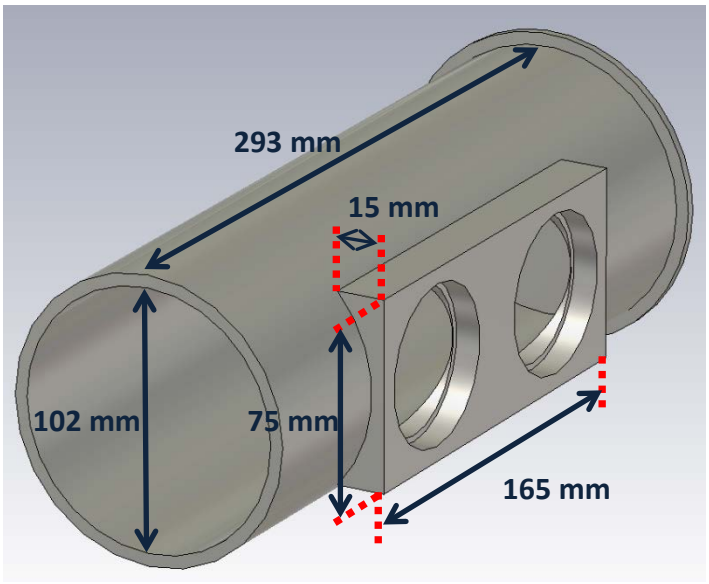

Fig. 4.3: Dimensions of C-GMS metal body

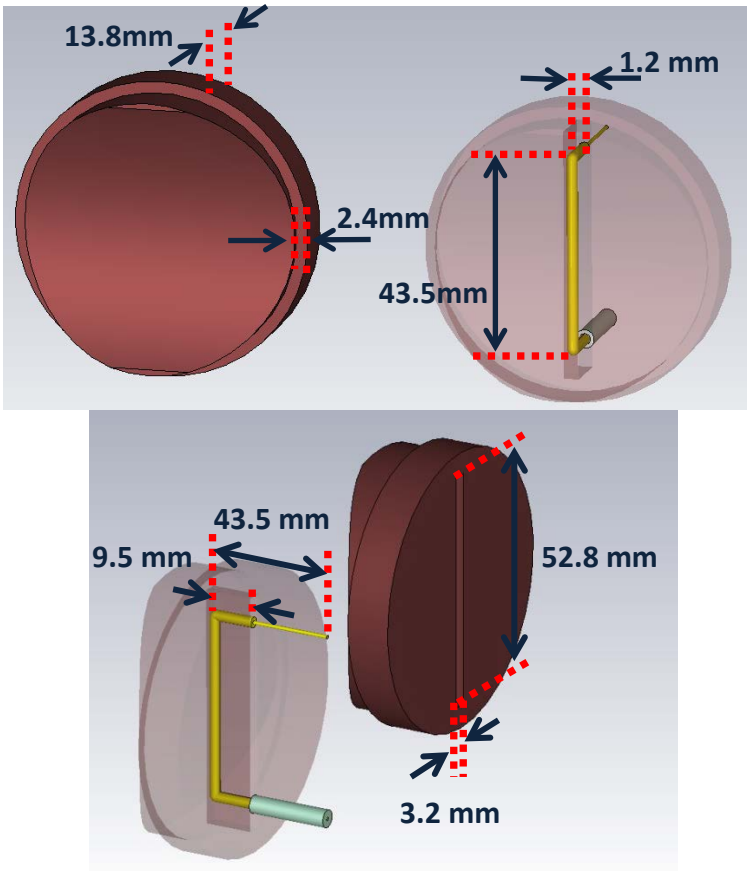

Fig. 4.4: Dimensions of C-GMS process seals and coupling loop

4.2.1 Simulation Setup of C-GMS with Air

The same frequency range, boundary conditions, solver type, and solver conditions were set for the C-GMS as for the R-GMS. As can be seen in Figure 4.5, the C-GMS filled with air consisted of 2,577,120 mesh cells when the lines per wavelength feature was 30. The value assigned to this feature defines the minimum number of mesh lines in each coordinate direction that are used for a distance equal to this wavelength. It essentially determines the quality of the results by setting the spatial sampling rate for signals inside the structure; a higher value will take longer to run but will provide better results. This feature becomes important in later simulations when the C-GMS is filled with material other than air, which would make the project too large to run on a desktop. Also, simulation time was halved by imposing a symmetry condition on the S_{11} and S_{22}. This simulation took 9 hours, 15 minutes and 35 seconds to run to completion, although the steady-state condition was not met and the energy in the system only reached the -38 dB point.

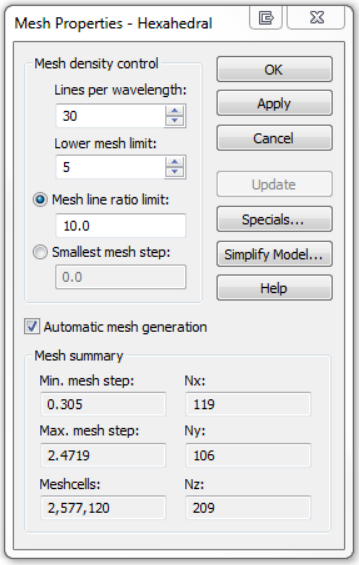

Fig. 4.5: Mesh setting for C-GMS filled with air

4.2.2 Simulation Results of C-GMS with Air

The simulation and measurement results agree fairly well for the C-GMS filled with air in Figure 4.6. As mentioned in the previous section, S-parameter symmetry was imposed on the system, so only the S_{11} and the S_{21} are shown. The cutoff frequency from Figure 4.6(b) is at 1.7 GHz, and the higher frequency content is very noisy due to the steady-state response not being met.

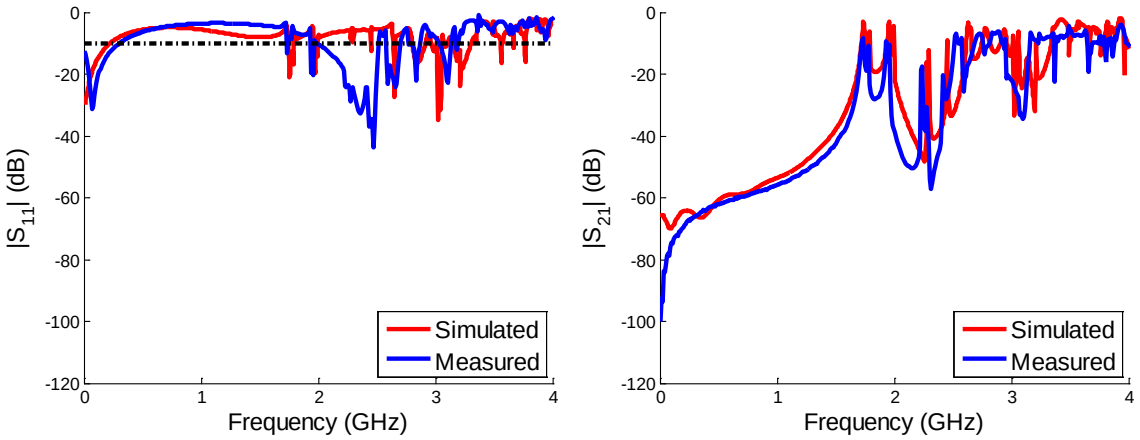

Fig. 4.6: C-GMS filled with air: a) S_{11} response b) S_{21} response

4.2.3 Explanation of Theory for C-GMS with Air

To verify that my simulation and measurement results agree with the theory, I calculated the cut-off frequencies of wave modes in the C-GMS. Equation (4.1) from Pozar was used to determine the cutoff frequency based upon the roots and the radial dimension given that "a" is 5.1 cm [13]. Circular waveguide theory states that the first TE mode to propagate is the mode with the smallest root, which is the TE_{11} mode in this case

$$f_{c_{nm}} = \frac{p'_{nm}}{2\pi a\sqrt{\mu\varepsilon}} \tag{4.1}$$

Thus, the TE_{11} mode is the dominant mode for the circular waveguide, and according to Table 1 the cutoff frequency should be 1.724 GHz for an air-filled C-GMS.

Table 1: Calculated cutoff frequency for circular waveguide filled with air

Mode	p'_{nm} (roots)	Cutoff Frequency (GHz)
f_{11}	1.841	1.724
f_{21}	3.054	2.859
f_{01}	3.832	3.587
f_{12}	5.331	4.991
f_{22}	6.706	6.278
f_{02}	7.016	6.568
f_{13}	8.536	7.991
f_{23}	9.970	9.334
f_{03}	10.174	9.525

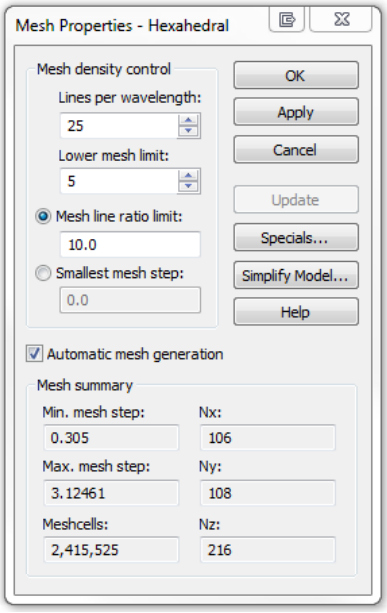

Fig. 4.7: Mesh Setting for C-GMS Filled with Oil

4.2.4 Simulation Setup of C-GMS with Vegetable Oil

The C-GMS with vegetable oil used the CST Debye model properties as described in section 3.2.4. Since the oil case increased the size of the project tremendously, I decreased the number of lines per wavelength to 25 to reduce the size of the model. Using the mesh setting in Figure 4.7, the size of the model was 2,415,525 mesh cells and it took 53 minutes and 18 seconds to run to completion.

4.2.5 Simulation Results of C-GMS with Vegetable Oil

Figure 4.8 *shows* that the results *for the C-GMS with oil are a lot* smoother since the project ran to completion. The first mode occurs at about 1.01 GHz for the simulation and 1.07 GHz for the measurement. The presence of the partially lossy oil helps to minimize the effect of multipath within the waveguide chamber, and any signals that reflect off the chamber walls are attenuated. This in turn produces a smoother graph.

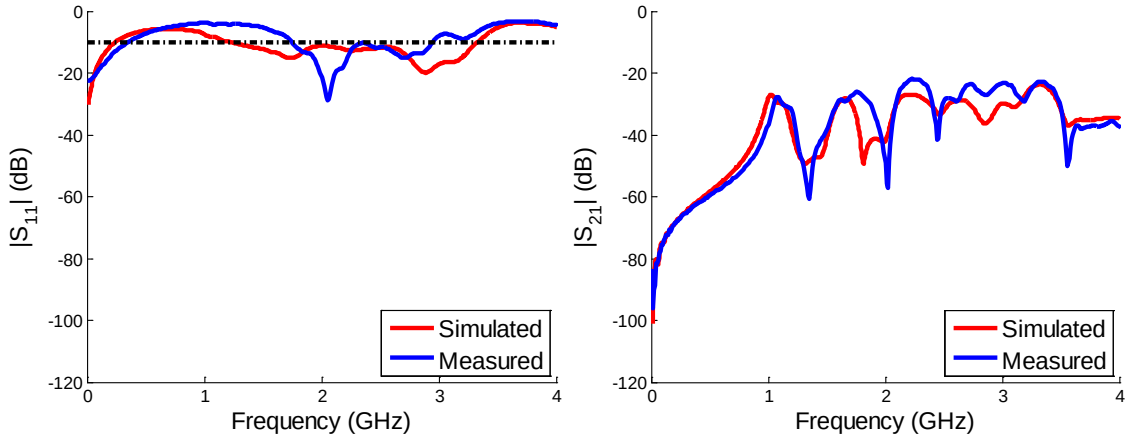

Fig. 4.8: C-GMS Filled with Vegetable Oil: a) S_{11} response b) S_{21} response

4.2.6 Explanation of Theory for C-GMS with Vegetable Oil

Table 2 was created using the same procedure as in section 4.2.3 for determining the cutoff characteristics for the C-GMS filled with vegetable oil. The expected cutoff frequency of 0.978 GHz is close to what was achieved experimentally. Comparing Figure 9 to Table 2, the f_{11}, f_{01}, f_{12} and f_{22} modes seem to show up very close to where they are expected to be, although it is a little harder to pinpoint the presence of the rest of the modes as precisely.

Table 2: Calculated cutoff frequency for circular waveguide filled with oil

Mode	p'_{nm} (roots)	Cutoff Frequency (GHz)
f_{11}	1.841	0.978
f_{21}	3.054	1.621
f_{01}	3.832	2.034
f_{12}	5.331	2.830
f_{22}	6.706	3.560
f_{02}	7.016	3.724
f_{13}	8.536	4.531
f_{23}	9.970	5.293
f_{03}	10.174	5.401

4.2.7 Simulation Setup of C-GMS with Water

Much like with the oil case, the presence of water inside the C-GMS adds considerably to the amount of mesh cells in the model. Figure 4.9 shows how the lines per wavelength value was set to 15, but the number of mesh cells for the entire project was still large – 21,763,566 mesh cells. The project took 43 hours and 36 minutes to run.

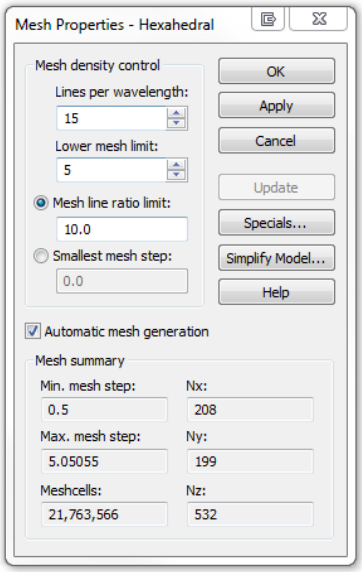

Fig. 4.9: Mesh Setting for C-GMS Filled with Water

4.2.8 Simulation Results of C-GMS with Water

As expected, the cutoff frequency shifted lower in frequency, and most of the modes are concentrated in the lower frequencies, particularly under 1 GHz. Figure 4.10(a) shows how the radiation characteristics are good when water is the impedance match, and Figure 4.10(b) illustrates the concentration of the modes in a dense space. The simulation follows the measurement pretty well as far as predicting where the modes will

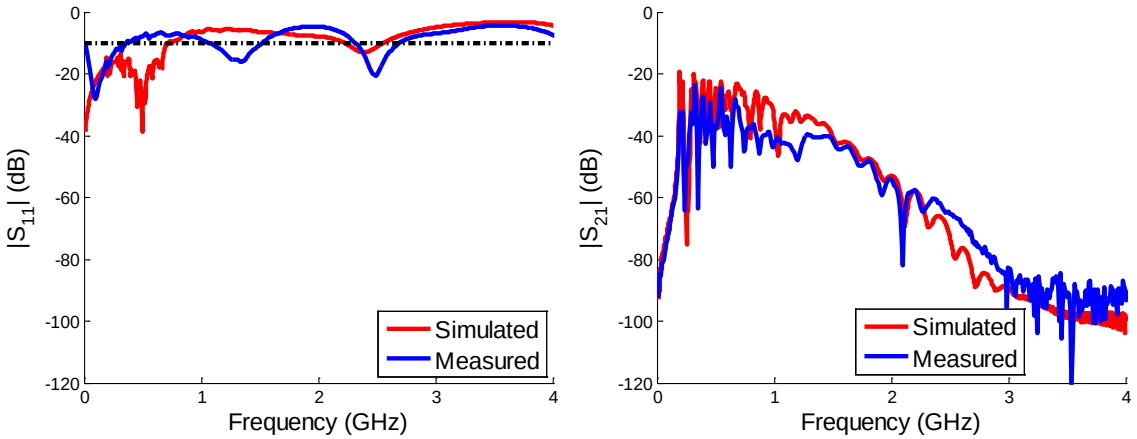

Fig. 4.10: C-GMS Filled with Water: a) S_{11} Response b) S_{21} Response

appear, so I have confidence in the lower frequency predictions of the model. A challenge for post-processing work for a circular GMS with high dielectric materials like water will be to determine how to extract information from the spectrum when the modes are concentrated in a small space. If the post-processing technique relies on identifying individual modes, I recommended using a rectangular GMS instead since the modes would be further spaced apart.

4.2.9 Explanation of Theory for C-GMS with Water

Comparing Tables 1, 2 and 3, all the modes shift lower, much like was explained throughout chapter 3. Graphically, this means that it is expected that most of the modes will be concentrated in the lower frequencies below 1 GHz.

Table 3: Calculated cutoff frequency for circular waveguide filled with water

Mode	p'_{nm} (roots)	Cutoff Frequency (GHz)
f_{11}	1.841	0.192
f_{21}	3.054	0.318
f_{01}	3.832	0.399
f_{12}	5.331	0.555
f_{22}	6.706	0.698
f_{02}	7.016	0.729
f_{13}	8.536	0.888
f_{23}	9.970	1.037
f_{03}	10.174	1.058

4.3 C-GMS with Oil and Water Binary Inhomogeneous Solutions

From sections 4.2.1 to 4.2.9, the homogeneous medium results paired the measurement to the simulation fairly well. Comparing the R-GMS results to the C-GMS results, it is clear that the R-GMS model performed better overall. Whereas the C-GMS simulation and measurement data match fairly closely, it would appear that the inherent nature of the circular waveguide makes it more difficult to interpret modes which are packed closer together.

The investigation into the C-GMS continues with the binary inhomogeneous solutions. The three water and oil solutions are summarized in Figure 4.11. The 25% water and 75% oil solution from Figure 4.12 reveals the presence of the water, but it is not as distinct as it was with the R-GMS; this is because the probes are almost entirely covered with the oil.

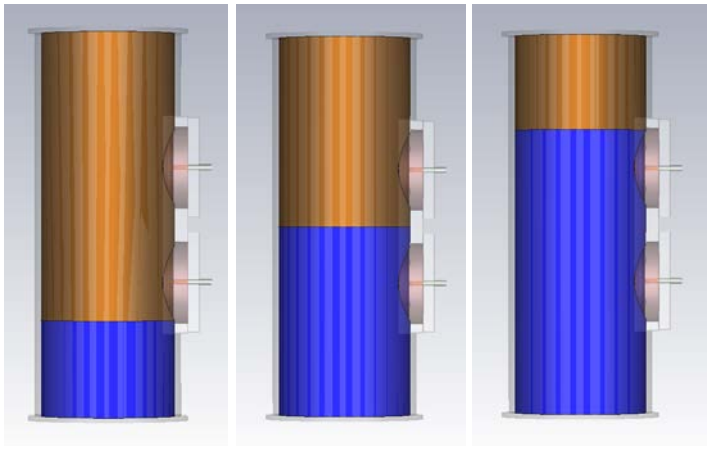

Fig. 4.11: Different Water and Oil Solutions: a) 25% water, 75% oil, b) 50% water, 50% oil, c) 75% water, 25% oil

For the 50% water and 50% oil case in Figure 4.13, the amplitude of the signal has been decreased due to the increased presence of water. The couplings loops are exposed to both materials, so the properties of both the oil and water are evident. The

discrepancy between the simulation and measurement is fairly pronounced above 1.5 GHz, but generally the match is not completely satisfactory. The rectangular GMS did a much better job of identifying the 50% water – 50% oil solution.

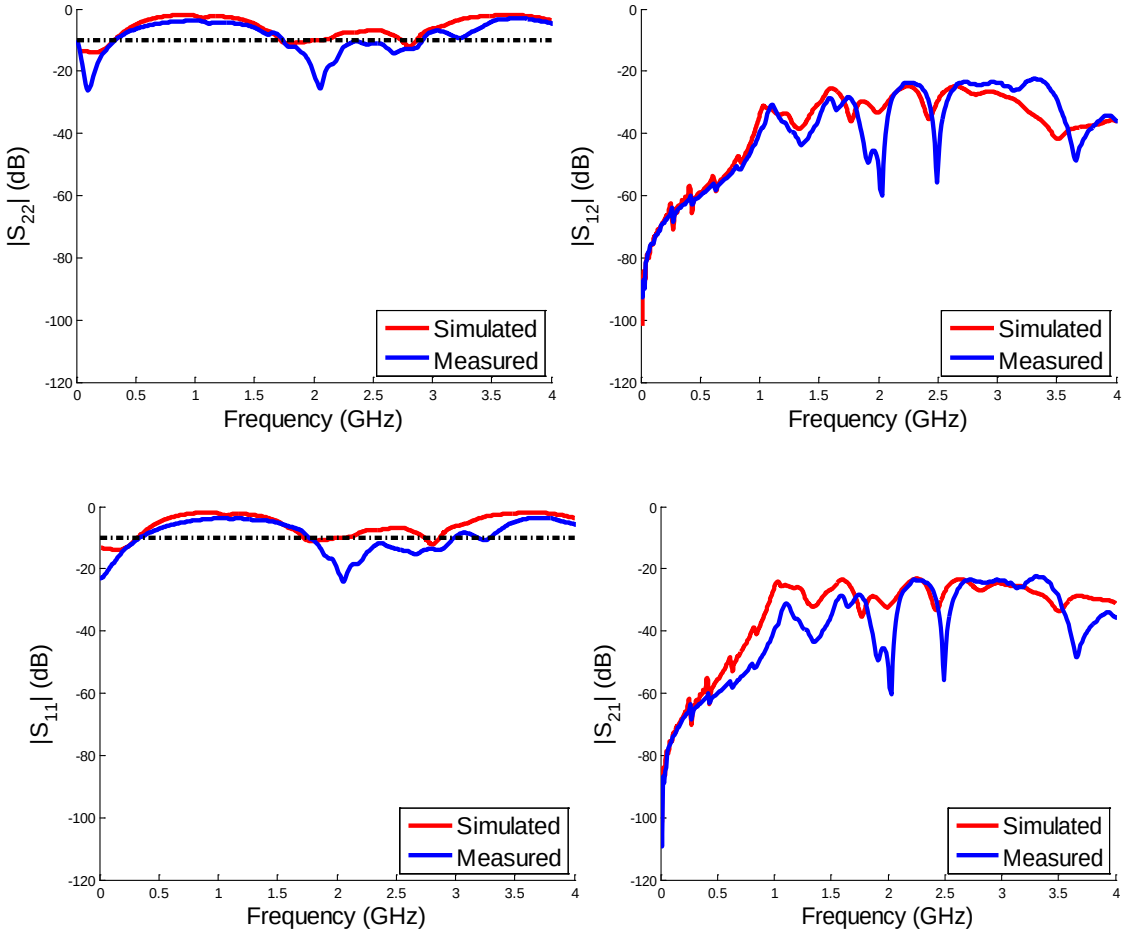

Fig. 4.12: C-GMS with 25% water, 75% oil. Clockwise, from top left: a) S_{11} , b) S_{21} , c) S_{22} , d) S_{12}

For the 75% water and 25% oil case in Figure 4.14, the simulation compares much better to the measurement for both the reflection ($S_{11}$and S_{22}) and the transmission (S_{12} and S_{21}) responses. Again, there may be some difficulty in interpreting the graphs

due to the closeness of many of the modes, but other than this difficulty, the graphs align much better than with the previous water-oil solution.

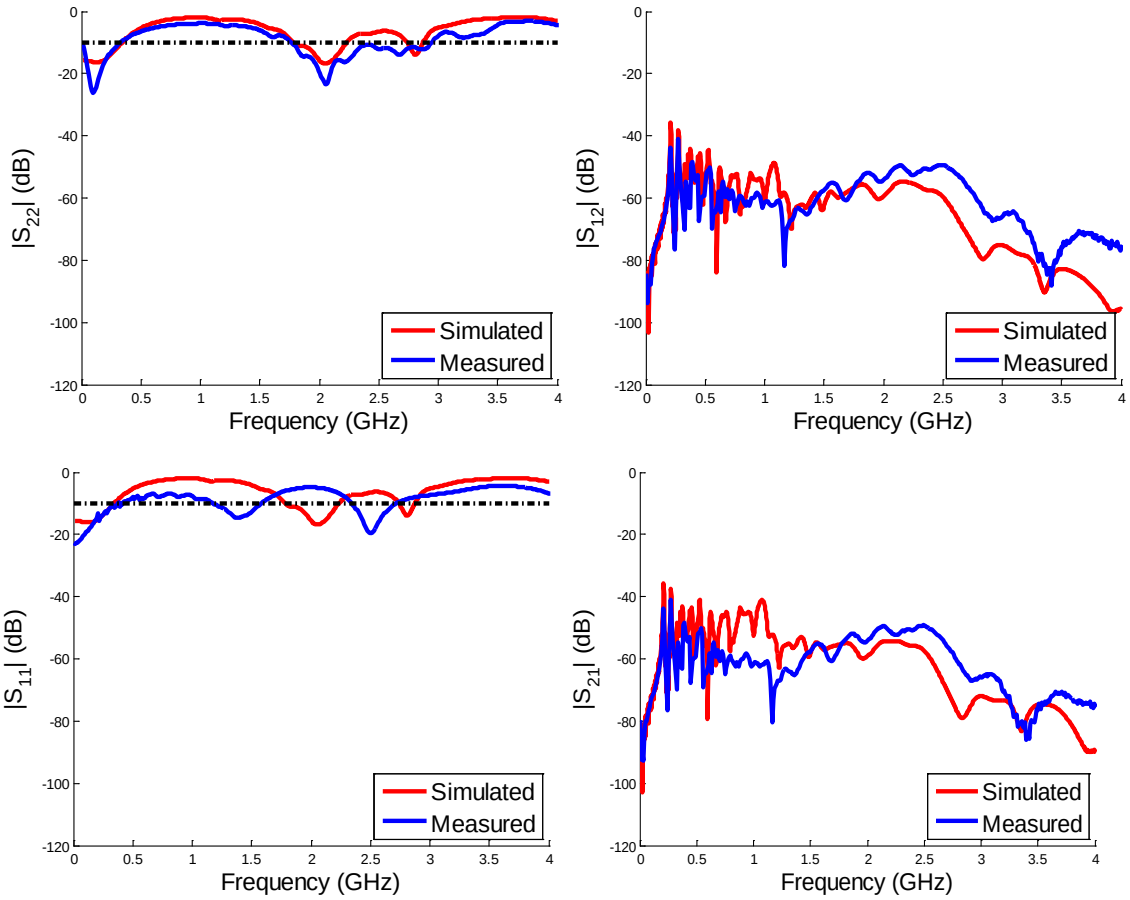

Fig. 4.13: C-GMS with 50% water, 50% oil. Clockwise, from top left: a) S_{11} , b) S_{21} , c) S_{22} , d) S_{12}

4.4 C-GMS Parametric Studies

The C-GMS parametric studies look at changing the circular GMS dimensions, the process seal dimensions, and the coupling loop shape. I also explore the placement of the ports to see how the current side-by-side arrangement of the ports compares to alternative locations, such as increasing the distance between them.

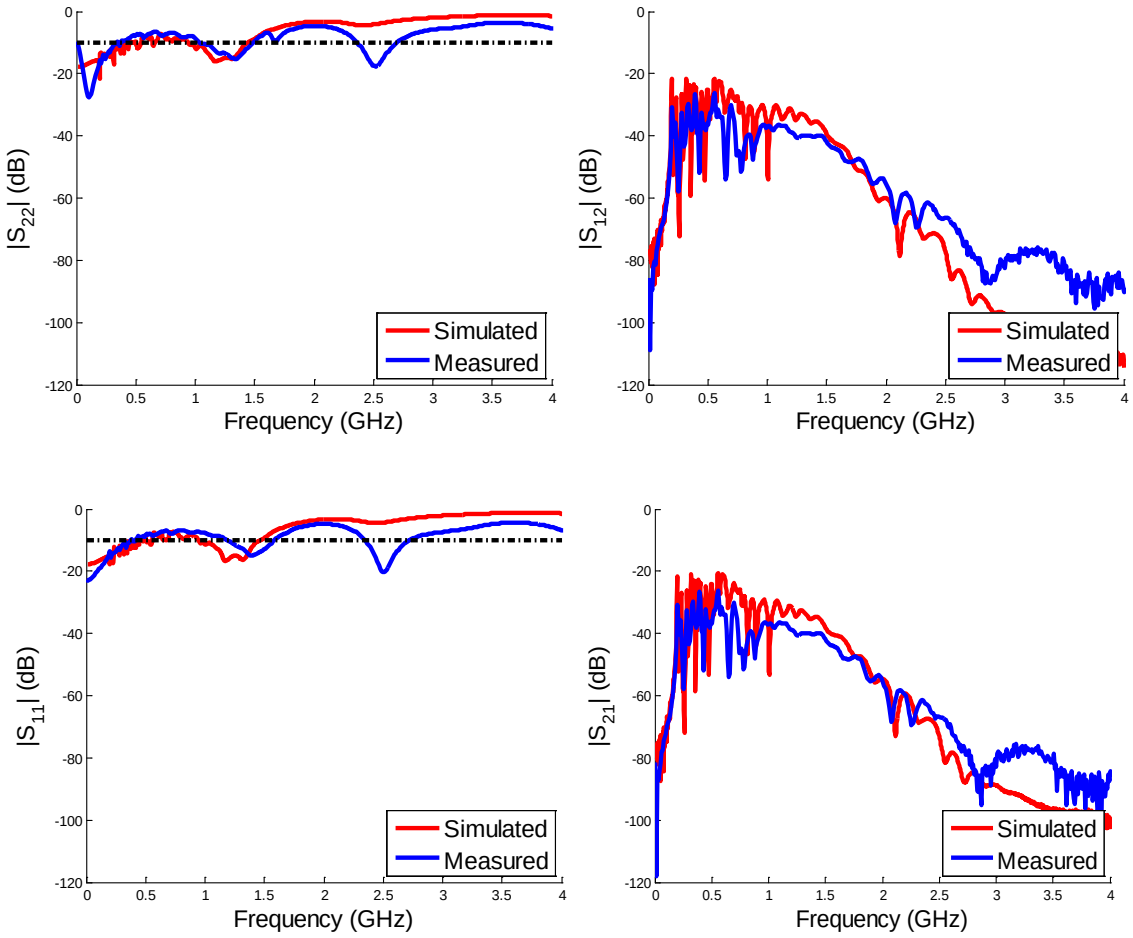

Fig. 4.14: C-GMS with 75% water, 25% oil. Clockwise, from top left: a) S_{11} , b) S_{21} , c) S_{22} , d) S_{12}

4.4.1 Modifying the Distance Between the Process Seals

The first parametric test is adjusting the spacing between the process seals. Moving the process seals further apart requires the energy to travel through more medium before being received by the second port, and thus it would seem natural for the signal to be attenuated more across the spectrum. From Figure 4.15, the spectrum attenuates mainly in the cutoff region. The passband region experiences some different standing wave patterns as the coupling loop position changes inside the closed chamber.

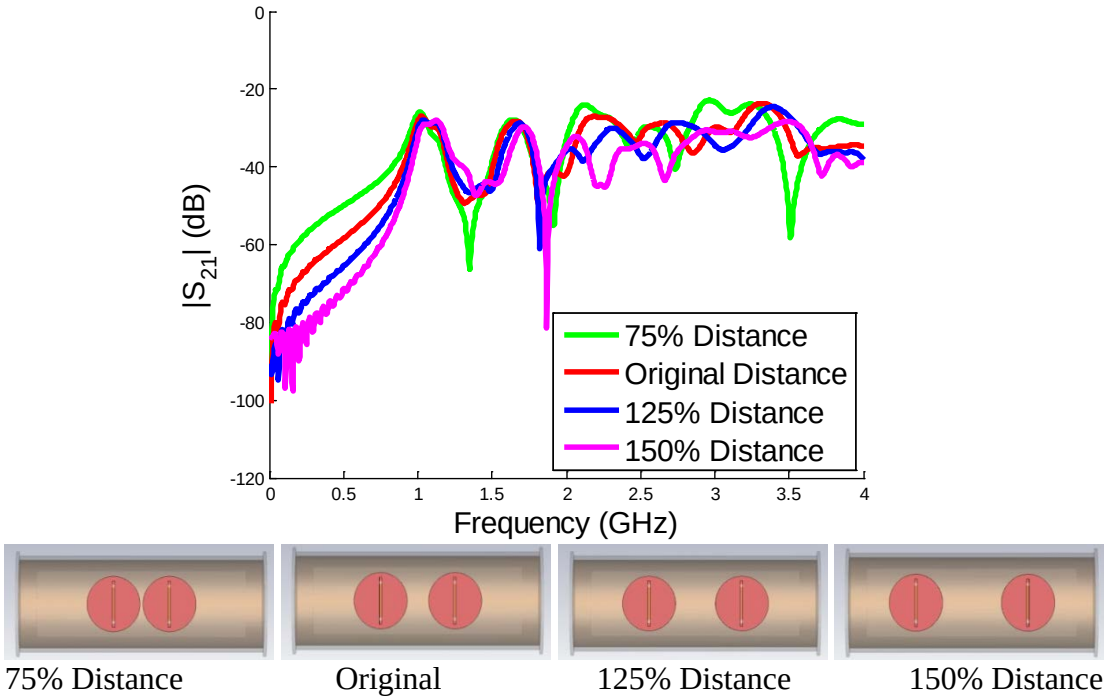

Fig. 4.15: Modifying C-GMS Process Seal Distance

4.4.2 Modifying the C-GMS Radius

The next parametric study is determining how the transmission response changes when the pipe radius is altered. The motivation for this is to consider what happens when, in an industrial setting with process flow pipes, a different size C-GMS for different pipe sizes. Circular waveguide theory says that the cutoff frequency will change, and I wanted to see to what degree this tool can demonstrate that. As Figure 4.16 shows, the cutoff frequency shifts lower as the pipe radius gets bigger, but it is interesting that the value of the first mode gets attenuated with increased radius. This may most likely be because the input signal takes longer to reflect off the back wall to get to the receiving port in a larger pipe, thus diminishing the signal strength.

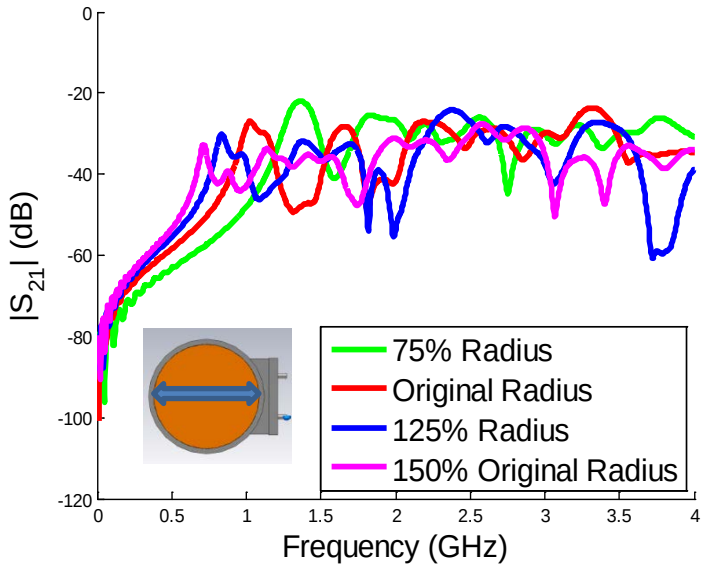

Fig. 4.16: Modifying C-GMS Radius

4.4.3 Modifying the C-GMS Length

The purpose of this study was to see the effects of placing of the C-GMS in different pipe-length scenarios. From Figure 4.17, as the pipe length is increased the standing wave pattern inside the chamber was changed, which is indicated by the different passband responses for all the different sizes. In retrospect, a better study would be to not have end caps and simulate pipe lengths as would be found in industrial settings.

4.4.4 Modifying the Coupling Loop Structure

The process of modifying the coupling loop structure from Figures 4.18 and 4.19 follows in the same manner as was done in the R-GMS case. Due to the very similar nature of the R-GMS coupling loop and the C-GMS coupling loop, the conclusions are virtually the same. The current coupling loop is not an efficient broadband antenna and future research should focus on redesigning it.

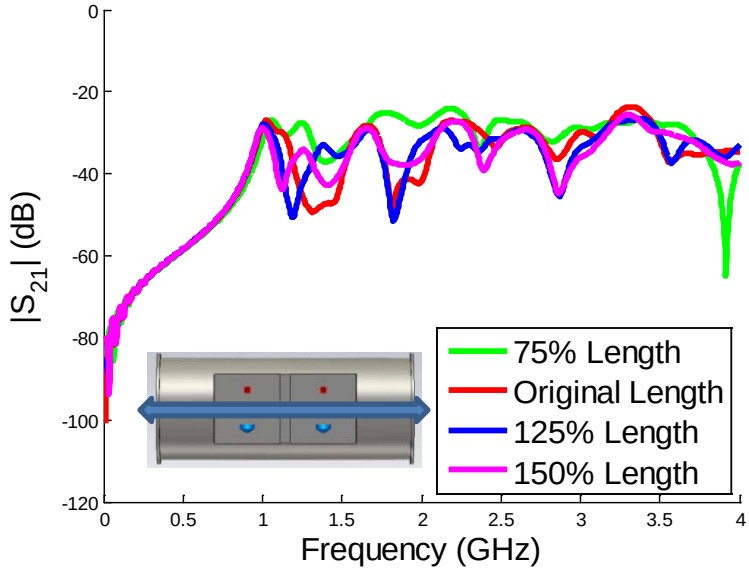

Fig. 4.17: Modifying C-GMS Length

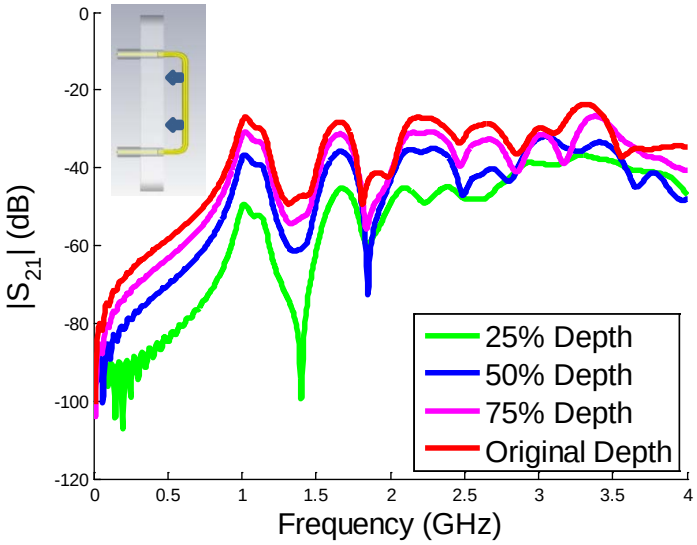

Fig. 4.18: Modifying C-GMS Coupling Loop Depth

4.5 Modifying the Port Position for the C-GMS

The purpose of this portion of the research was to identify the significance of placement of the ports at different locations. In these simulations, it is desirable to see if energy can be better transferred through optimal placement of these ports, if such an

optimal position even exists. The first setup involved rotating one of the ports 180° to the other side of the pipe, as in Figure 4.20(a); this idea stemmed from curiousity in seeing what happens if energy gets transferred across and relying less on backscatter. The results of this new orientation were compared to the original position simulated and displayed in Figure 4.20(b).

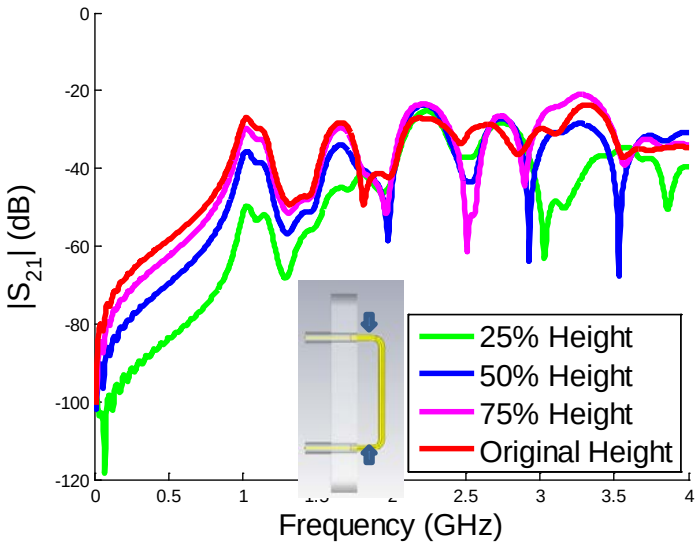

Fig. 4.19: Modifying C-GMS Coupling Loop Height

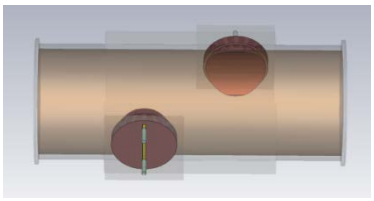

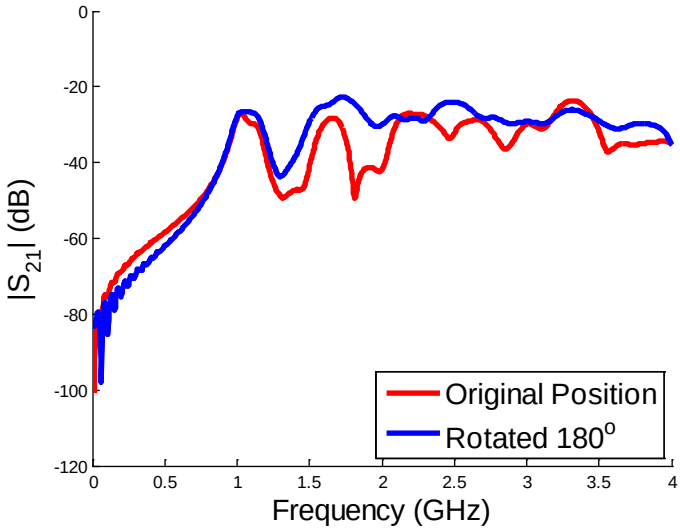

Fig. 4.20: a) Rotating port 180° on C-GMS, b) Spectra for rotating port 180° on C-GMS

The results for this new orientation has a smoother passband response, but it is not clear whether this means that information about the material is lost or not since the mode action becomes less obvious. Another thing to consider is that this design is not very practical to manufacture, so considering that the results do not deviate much it does not make much sense to implement this design.

Two other designs were explored, each with the goal of seeing what happens if both ports are aligned along the same pipe-length direction, and rotated at 90° and 180°. Although the microwave energy travels down the pipe, I was just curious to see what happens when the ports face each other as in the R-GMS design. As in Figure 4.21(a), the ports were aligned along the pipe radius separated by 90° of space. I expected to see some similarity in the spectral response of this compared to the original position of the two ports (where they were in line down the length of the pipe), although there are certain considerable differences. There is a lower prominence of the first mode, and see how the second mode has more dominant characteristics. Although the cutoff frequency is still the

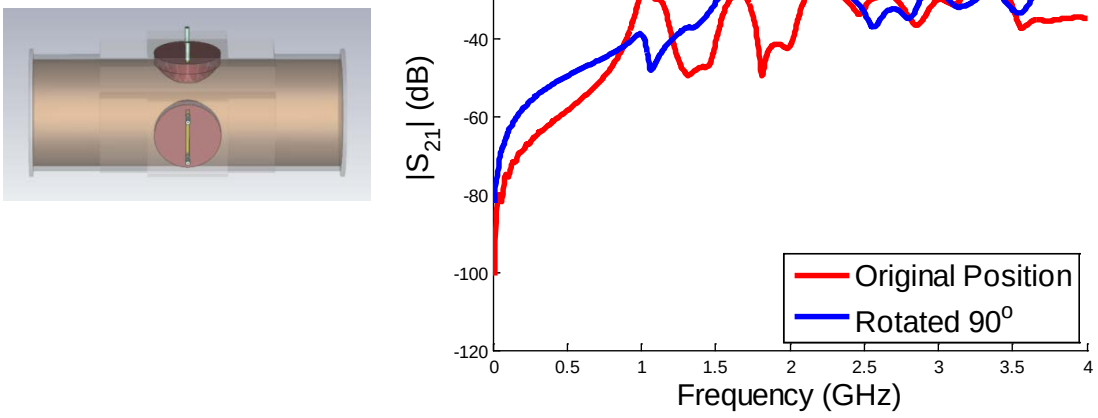

Fig. 4.21: C-GMS new port position, rotating port 90°: a) Design, b) Spectra

same, due to the reduced emphasis of the first mode, it would almost seem that the cutoff region extends to where the second mode is.

The second orientation is similar to the first, with the exception that the second port is fully across the pipe at 180°. This is remniscent of the R-GMS port placement, and I highly expected the material properties to look similar to the results of the R-GMS oil case. Figure 4.22b illustrates that the new response is much smoother than the original design, with only a few very prominent nulls occuring. These nulls, when compared to Table 2, do not appear where one would expect them to be for the higher modes, but the signal strength is certainly stronger due to the ports being directly across from each other.

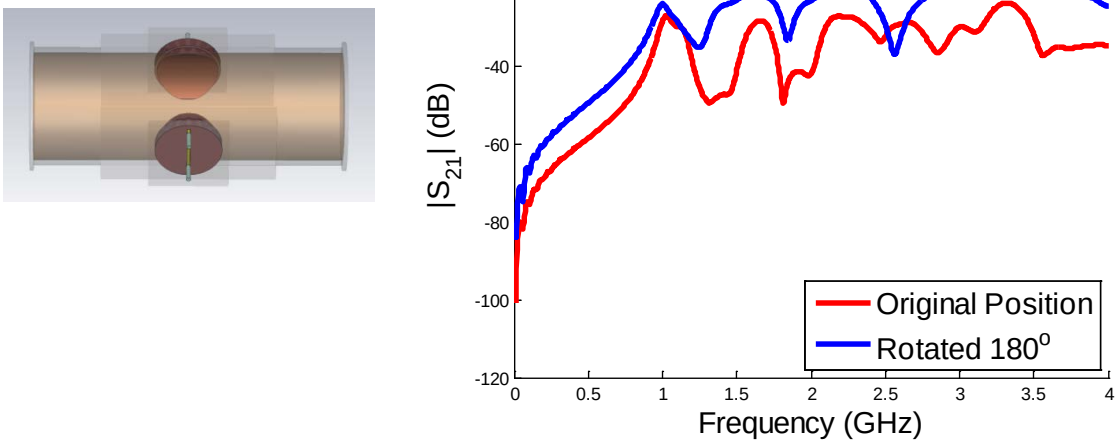

Fig. 4.22: C-GMS new port position, rotating port 180°: a) Design, b) Spectra

CHAPTER FIVE

Conclusion and Future Work

This work culminates with valuable and practical software models for the future design and study of Guided Microwave Spectrometry systems. Previous to the availability of computational numerical software, the process of developing this novel measurement system for new applications had been time consuming and costly. The objectives for this work were to use CST as a tool to develop a new system at a significantly lower cost and at a faster pace than previously, and these objectives were met with great success. The performance of both the rectangular and the circular GMS models are very close to the performance of their counterparts in the laboratory, which demonstrates the reliability of these models.

I am especially satisfied with the rectangular GMS model, where the spectra results for each of the six different MUT scenarios matched very well. The GMS width and length studies illustrated that changing the width caused the cutoff frequency to change and changing the length affected the attenuation in the cutoff region. Changes in the width of the process seal have virtually no impact in the signal across the entire frequency range, whereas changing the height of the process seal revealed that above 2.5 GHz the coupling loop failed to perform well. Changing the process seal permittivity also confirmed that the coupling loop is a primary source of error within the system, and the ideal waveguide port benchmark proved that the current design does not perform very well.

Much like the rectangular GMS, the circular GMS software model performed similarly to the experimental laboratory results. One of the primary observations for the spectra across all the different material types is that, due to the inherent nature of the circular waveguide, the modes are clustered closer together. The round design of this measurement system lends itself to fit pipes more easily without the need for transition segments; however, in a situation where greater spacing between the modes would be desirable, it would be better to use a rectangular measurement system. The parametric study for this structure confirmed that the radius of the pipe is solely what influences the cutoff frequency; larger radius pipes have a lower cutoff frequency with a more attenuated signal. For the port arrangement study, it would appear that the current in-line process seal design would remain the optimal design choice for this sensor unit as the other port variations provided minimal changes in the spectral response.

The design process has been improved with the availability of these tools, giving significant advantages over the previous cut and try methods of designing a GMS system for a particular application. The benefits are cost reduction and decreased design time, while also giving the unprecedented ability to understand the individual qualities of each of the components. Previously, there was no way to isolate the effects of each of the parameters to identify which spectra behavior corresponded to each component. Future adaptation of the GMS to new applications has thus been made more efficient and brings an added dimension of understanding the particular electromagnetic effects of each of the components, which gives great value to this tool.

The success of the two models is a good start for future research that could be continued to improve this tool. All the research to date has been with pure homogeneous

medium (air, oil, water) and binary inhomogeneous solutions (oil and water combined), but future research could investigate more complex non-homogeneous materials such as concrete. Another point of study could be to redesign the coupling loop structure and to find better ways to maximize the energy transfer into and out of the system. Finally, it would be useful to observe the more realistic scenario of randomized material flow through a pipe with a GMS attached, as opposed to the controlled studies which have looked at static material measurements.

BIBLIOGRAPHY

[1] Balanis, Constantine A. *Advanced Engineering Electromagnetics*. New York: Wiley, 1989. Print.

[2] Jean, B.R. "Process Composition Monitoring at Microwave Frequencies: A Waveguide Cutoff Method and Calibration Procedure." *IEEE Transactions on Instrumentation and Measurement* 55.1 (2006): p. 180-86. Print.

[3] Jean, B.R. "Guided Microwave Spectrometry for In-line Analysis of Flowable Materials." *Sensors Update* 7.1 (2000): p. 171-84. Print.

[4] CST Microwave Studio 2012 Edition.

[5] GE Engineering Thermoplastics. *ULTEM: PEI Resin*. Pittsfield: GE Engineering Thermoplastics, 2003. Print.

[6] Agilent 85070E Dielectric Probe Kit, Agilent Technologies, 200MHz-50GHz.

[7] 85070 Version E06.01.36 Copyright 1989-2012 Agilent Technologies.

[8] Agilent Technologies PNA-L Network Analyzer; N5230C; 300 kHz – 13.5 GHz

[9] MATLAB Version 7.12.0.635 (R2011a).

[10] von Hippel, A. *Dielectrics and Waves.* Boston, MA: Artech House, 1995: p. 95, 175.

[11] Agilent Technologies ENA Series VNA; E5071B; 300 kHz – 8.5 GHz.

[12] Balanis, C.A., Advanced Engineering Electromagnetics; Tempe, AZ: John Wiley & Sons, Inc, 1989, p. 357.

[13] Pozar, David M. *Microwave Engineering*. Hoboken, NJ: J. Wiley, 2005: p. 119-120. Print.